A Novel Modeling Framework for Stator Inter-Turn Fault Analysis in Traction Permanent Magnet Synchronous Motors

by

Feng Zhou

A dissertation submitted in partial fulfillment
of the requirements for the degree of
Doctor of Engineering
(Automotive Systems and Mobility)
in The University of Michigan-Dearborn
2025

Doctoral Committee:

Associate Professor Taehyung Kim, Chair
Associate Professor Sang-Hwan Kim
Associate Professor Junho Hong
Junwoo Kim, LG Electronics

Feng Zhou

fengzho@umich.edu

ORCID ID: 0009-0000-0522-6007

Copyright © Feng Zhou 2025

To My Family,

My Loving Wife, Yue Dong

and My Daughters, Ayrn and Haley.

Acknowledgements

Through the course of this doctoral journey, I have been fortunate to receive guidance, support, and encouragement from many individuals. Completing this dissertation would not have been possible without their kindness, generosity, and love.

First and foremost, I would like to express my deepest gratitude to my advisor, Dr. Taehyung Kim. He has guided me since my master's studies at the University of Michigan–Dearborn, offering unwavering support, insightful advice, and career guidance over the years. His mentorship has been instrumental throughout my academic and professional development. This work could not have been completed without him.

My sincere thanks also go to my former colleagues and friends at LG Electronics, Junwoo Kim, Hyunseok Son, and Dongcheol Lee, with special appreciation to my former team leader, Junbo Yun. Their encouragement and support during my time at LG played a vital role in setting me on the path to pursue this higher degree.

I would like to thank Akhila for applying her expertise in machine learning to train a complementary model that helped validate my approach. Her contribution was essential in demonstrating the advantages of work in this theses.

Most importantly, I owe my deepest gratitude to my family. Pursuing a doctoral degree while working full time would not have been possible without their unwavering support. My wife has made countless sacrifices to help me through this journey, and I am forever grateful. I am also profoundly indebted to my parents, without their love, care, and encouragement, none of this would have been possible.

Table of Contents

Dedication iii

Acknowledgements iv

List of Tables viii

List of Figures ix

Glossary of Symbols xii

Abstract xiv

Chapter 1 Introduction 1

1.1 Overview 2

1.2 Progression in Traction Electric Machine Technology 3

1.3 Stator Winding Insulation Failures 3

1.4 Problem Statement 5

1.5 Dissertation outline 6

Chapter 2 Overview of Modeling Approaches for Permanent Magnet Synchronous Machine 8

2.1 Stator Voltage Equation Based Modelling Approach 9

2.1.1 Space Vector Based Derivation Method 10

2.1.2 Phase Variable Equivalent Circuit Based Derivation Method 11

2.2 State-space Representation of Stator Voltage Equation Based Model 11

2.3 Flux Linkage Based Magnetic Domain Model 13

2.4 Final Element Method (FEM) Based Model 15

Chapter 3 Overview of Phase Winding Inter-turn Short Fault Detection Techniques 18

3.1 Symmetrical Components 19

3.2 Fault Indicators 22

3.2.1 Fundamental Negative Sequence Voltage 23

3.2.2 Fundamental Zero Sequence Voltage 24

3.2.3 Second Order Harmonic in the d-axis Current 25

3.2.4 Second Order Harmonic in the Three-phase Current 26

3.3 Signal Processing Techniques for Fault Detection 27

3.3.1 Short Time Fourier Transformation (STFT) Turn Fault Detection 28

3.3.2 Wavelet Transformation (WT) Turn Fault Detection 29

Chapter 4 PMSM Theoretical Framework 31

4.1 Governing Voltage Equations of SPMSM Stator Windings 33

4.1.1 Healthy SPMSM Governing Voltage Equations 33

4.1.2 Healthy IPMSM Governing Voltage Equations 36

4.1.3 Inter-turn Short Fault SPMSM Governing Voltage Equations 39

4.1.4 Inter-turn Short Fault IPMSM Governing Voltage Equations 46

4.1.5 PMSM Torque Equation Development 51

4.2 SPMSM Modeling within Simulink-Simscape Environment 52

4.2.1 Simulink-Simscape Language Structure 53

4.2.2 SPMSM Simscape Component Modeling 55

Chapter 5 PMSM Control Strategy and Stator Turn Fault Simulation Controller Design 58

5.1 Field-oriented Control (FOC) 60

5.2 Operation Region of PMSM in Current Plane at d-q Reference Frame 63

5.2.1 Maximum Torque per Ampere (MTPA) MTPV Control, Flux Weakening 68

5.3 Pulse-width-modulation (PWM) Strategies 71

5.3.1 Space Vector PWM (SVPWM) 72

5.3.2 Discontinuous PWM (DPWM) 76

5.4 Issue with Open-loop-controlled PMSM Simulation 77

5.5 Close-loop-controlled SPMSM Simulation Model and Results 79

Chapter 6 Machine Learning Model Training 86

6.1 Comparative Evaluation of CNN, Random Forest, and XGBoost for PMSM Fault Diagnosis Using Idc and Multi-Current Signals 87

Chapter 7 Conclusion and Recommended Future Work 91

6.1 Conclusions 92

6.2 Contributions 93

6.3 Recommended Future Work 95

References 97

Appendices 104

List of Tables

No.	Title
Table 5.1	VSI space vector switching states
Table 5.2	Parameters of proposed simulation model

List of Figures

No.	Title
Figure 1.1	Examples of common three-phase machine stator winding failure [3]. (a) Winding shorted turn-to-turn. (b) Winding shorted phase-to-phase. (c) Winding with shorted coil. (d) Winding grounded at edge of slot.
Figure 2.1	Simscape PMSM magnetic domain model [9].
Figure 2.2	Representation of FEM modeling approach for PMSM [10].
Figure 3.1	Decomposition of three-phase system into symmetrical components.
Figure 3.2	Notation convention for symmetrical component quantities.
Figure 4.1	Equivalent Circuit of PMSM with inter turn short at phase-a.
Figure 4.2	Simscape code structure demo.
Figure 4.3	(a) Simscape component model of SPMSM (b) Zero-sequence-voltage calculation subsystem outside of the Simscape component model
Figure 5.1	Control block diagram of Field-Oriented Control (FOC) [37]
Figure 5.2	Voltage and current constraints of PMSM depicted in a current plane. (a) Interior permanent magnet synchronous machine (IPMSM). (b) Surface-mounted permanent magnet synchronous machine (SPMSM).
Figure 5.3	Voltage and current constraints of PMSM machine depicted in a current plane demonstrating speed effect

Figure 5.4 Operating regions according to the parameters of the permanent magnet AC machines.(a) IPMSM (Finite-speed drive system). (b) IPMSM (infinite-speed drive system). (c) SMPMSM(finite-speed drive system). (d) SMPMSM (infinite-speed drive system).

Figure 5.5 Illustration of SPWM generation by comparison of modulation signal [40]

Figure 5.6 Illustration of a common voltage source inverter (VSI) topology

Figure 5.7 Voltage space vectors and switching states of a two-level VSI

Figure 5.8 Illustration of space vector decomposition in switching states

Figure 5.9 Distorted abc-phase current from improper synchronized open-loop-controlled SPMSM

Figure 5.10 Overview of the Simulink control system with SPMSM model integrated

Figure 5.11 Model SVPWM controlled inverter gate signal

Figure 5.12 Result of the proposed simulation model at healthy condition.

Figure 5.13 Result of the proposed simulation model at 5% condition.

Figure 5.14 Result of the proposed simulation model at 15% condition

Figure 6.1 Receiver Operating Characteristic curve for CNN2 trained on (a) Idc only data (b) all currents data resampled to 1200 samples. Training and validation accuracy curves for CNN2 trained on (c) Idc only data (d) all currents data resampled to 1200 samples.

Glossary of Symbols

Symbol	Definition	Unit
Definition of Electrical and Magnetic Symbols		
i	: Instantaneous current	A
I	: Instantaneous current vector	A
v	: Instantaneous current	V
V	: Instantaneous current vector	V
L	: Inductance	H
M	: Mutual inductance	H
Z	: Impedance	Ohm
λ	: Instantaneous flux linkage	Wb
T	: Torque	Nm
ω	: Angular velocity in radian per second	rad/sec
θ	: Angle (rotating position)	rad

Definition of Subscripts

a,*b*,*c*	: *abc* reference frame	-
q,*d*	: *qd* reference frame	-
s	: SPMSM	-
i	: IPMSM	-
PM	: Permanent magnet	-

Abstract

This dissertation presents a novel modeling framework for analyzing stator inter-turn short-circuit faults in Permanent Magnet Synchronous Motors (PMSMs), tailored for developing reliable diagnostics for electric vehicle traction drives. Conventional simulation of faulted PMSMs often suffers from numerical instability and inefficiency. To overcome this, a robust and scalable model was developed in the Simulink-Simscape environment.

Leveraging an acausal, equation-based approach with an implicit DAE solver, the framework accurately captures fault dynamics within a closed-loop Field-Oriented Control (FOC) system, eliminating common algebraic loop issues that compromise accuracy.

Simulation results validated the model's ability to replicate key fault indicators, such as zero-sequence voltage and dq-axis current harmonics. The framework’s computational speed and scalability proved highly effective for generating large datasets, enabling the successful training of machine learning algorithms for robust, online fault detection using standard inverter signals.

Chapter 1

Introduction

1.1 Overview

On account of the fast-growing electric vehicle (EV) industry, traction permanent magnet AC (PMAC) machines have become one of the most extensively studied types of electrical machines. Amongst the key areas of investigation is the analysis and mitigation of stator winding faults, particularly inter-turn short-circuits faults, which often referred to as turn-to-turn fault. A stator turn fault in a PMAC machine arises when the insulation between adjacent turns in a stator winding fails, often due to thermal stress, mechanical vibration, or chemical degradation, resulting in a short circuit between two or more turns. Such a fault can escalate rapidly due to the high circulating currents generated in the shorted path, leading to localized overheating and further insulation breakdown. This, in turn, causes significant asymmetry in the otherwise balanced three-phase system, resulting in distorted control behavior and degraded machine performance. In safety–critical applications such as traction drives, these faults can have catastrophic consequences if not detected and addressed promptly.

As supported by various studies, inter-turn-short-circuit faults represent one of the earliest and most prevalent failure modes in electric machines [1]. Therefore, early-stage detection and preventive intervention are critical to maintaining the operational integrity of traction PM machines. This thesis proposed an innovative way to construct inter-turn fault PM machine simulation model that can be close-loop controlled by a current-controlled voltage source inverter (CCVSI) model for dynamic performance study. The model total run time is significantly faster than conventional simulation approach under complicated torque control command, which make the model suitable for future neural network fault detection training research.

1.2 Progression in Traction Electric Machine Technology

In the early stages of EV development, non-synchronous induction machines were a popular choice due to their robustness, mature technology, and cost-effectiveness. The increasing demand for more compact and cost-efficient EV architectures has shifted the industry's preference toward traction machine solutions with higher power density, such as Surface-Mounted Permanent Magnet Synchronous Machines (SPMSMs) and Interior Permanent Magnet Synchronous Machines (IPMSMs). Among the two, SPMSMs were predominantly used in early-generation EVs due to their structural, control simplicity and lower manufacturing cost. However, as IPMSM technology has matured over the years and costs have continued to decline, these machines are becoming increasingly favored for modern EV applications, owing to their superior performance characteristics, particularly in terms of torque production and efficiency across a wide speed range. Nowadays, OEMs increasingly adopt Interior Permanent Magnet Synchronous Reluctance Machines (IPM-SynRMs), a hybrid of Synchronous Reluctance Machines (SynRMs) and IPMSMs. This machine architecture leverages both the reluctance torque generated by the rotor's low-permeability flux paths and the electromagnetic torque from embedded permanent magnets. As a result, IPM-SynRMs can achieve competitive performance while significantly reducing the reliance on rare-earth materials, ultimately offering a more cost-effective and resource-efficient solution when properly designed.

1.3 Stator Winding Insulation Failures

Since all widely adopted traction machines today share a permanent magnet synchronous architecture, they are susceptible to a similar range of fault types, including stator winding faults, rotor demagnetization, and various mechanical failures. Among these, stator winding faults are

particularly critical, accounting for approximately 38% of all motor failures [2]. These faults are typically classified into inter-turn short circuits, open-circuit faults, phase-to-phase short circuits, and phase-to-ground faults. Among them, the inter-turn short circuit is the most prevalent. While potentially severe, it is largely preventable if identified in its early stages and addressed through timely diagnostic and mitigation strategies.

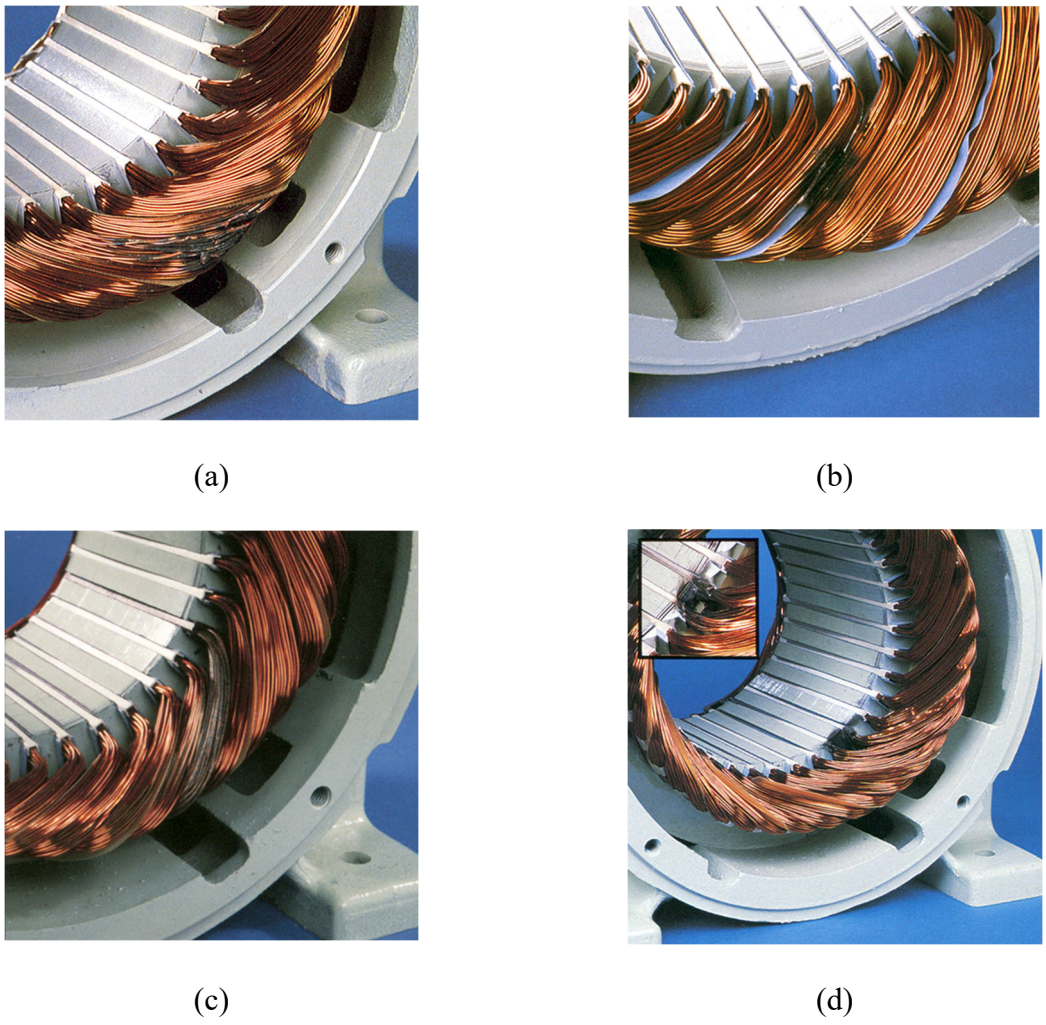

(a) (b)

(c) (d)

Figure 1.1 Examples of common three-phase machine stator winding failure [3]. (a) Winding shorted turn-to-turn. (b) Winding shorted phase-to-phase. (c) Winding with shorted coil. (d) Winding grounded at edge of slot.

A common inter-turn short occurs between adjacent stator windings within the same phase coil when the insulation between those turns degrades or fails. This type of fault creates a low-impedance path that allows circulating fault current to flow locally within the affected coil, even when the machine is operating under normal load conditions. Although the affected phase may still appear functional from a system-level perspective, the localized fault current can reach dangerously high levels, leading to rapid heating and concentrated magnetic distortion. These effects can further weaken the insulation, causing the fault to escalate into more severe conditions such as phase-to-phase or phase-to-ground faults. Inter-turn shorts are often caused by factors such as thermal stress, mechanical vibration, manufacturing defects, or electrical overstress. Early detection is essential, as these faults typically exhibit subtle electrical or thermal symptoms before developing into catastrophic failures. As such, inter-turn short circuits represent a critical reliability challenge in permanent magnet synchronous machines, particularly in high-performance traction applications.

1.4 Problem Statement

Given the previously discussed background, it is essential to address inter-turn short circuits at their earliest stage to prevent more catastrophic consequences. Therefore, a reliable online detection method that can be used while the vehicle is operating is required. Several prerequisites must be considered when implementing such methods. First, the detection algorithm must be highly reliable, as false positives may render the vehicle undriveable. Second, the method should leverage the existing hardware of the traction inverter, as modern EV development places significant emphasis on cost efficiency. Finally, the algorithm should achieve high sensitivity in detecting small faults while strictly preventing any false triggering.

To develop effective fault detection algorithms, simulation is often employed as a foundational tool. While numerous simulation approaches have been proposed in existing research, a model that focuses on numerical efficiency and scalability for fault scenarios has been merely explored. Such framework is essential for training machine learning-based fault detection models, as extensive datasets must be generated by repeatedly running simulations with different parameters and fault settings to ensure high model reliability. A further challenge in developing these models is that simulating PMSMs under fault conditions introduces significant numerical complexity. This often leads to cumbersome model structures and potential simulation errors, making it difficult to achieve both accuracy and speed.

This thesis proposes a novel modeling framework for stator inter-turn fault analysis in traction PMSMs. Theoretical foundations are established for both SPMSM and IPMSM machine types. A SPMSM model is developed within the Simulink–Simscape environment, and its simulation results are presented

1.5 Dissertation Outline

The background, motivation, and significance of this research are introduced in Chapter 1. Chapter 2 provides a literature review of existing inter-turn fault detection methods and modeling strategies for PMSMs, with a focus on their limitations in scalability and numerical efficiency. In Chapter 3, theoretical foundations for modeling inter-turn faults in both SPMSM and IPMSM machines are developed, including derivations of dq-axis voltage and torque equations. Chapter 4 presents a Simulink–Simscape based SPMSM model under inter-turn fault conditions, demonstrating high numerical efficiency and flexibility. Chapter 5 extends the modeling framework to include IPMSM dynamics and control, incorporating advanced features such as

MTPA and flux weakening strategies. A comprehensive closed-loop simulation framework integrating FOC and SVPWM is introduced in Chapter 6, enabling realistic fault behavior representation under dynamic operating conditions. In Chapter 7, the developed model is employed to generate datasets for machine learning training, and design considerations for achieving high fault sensitivity while avoiding false triggers are discussed. Chapter 8 outlines the experimental validation using a physical PMSM test bench, confirming model accuracy and detection performance in real-world conditions. Finally, Chapter 9 presents the conclusions, key contributions, and recommendations for future work.

Chapter 2
Overview of Modeling Approaches for Permanent Magnet Synchronous Machine

Despite the traditional approach of using a real PM machine and manually inducing faults in the stator winding to perform bench tests for inter-turn fault detection, this method is often considered labor-intensive and impractical. Accurately identifying the stator's neutral point and precisely controlling the shorted portion of the winding to investigate various fault behaviors can be particularly tedious and time-consuming [4]. Moreover, with the widespread adoption of hairpin winding machines for improving winding density, adjusting the shorted winding ratio on a test bench has become even more challenging. As a more efficient alternative, simulation-based methods have been developed, offering greater flexibility, control, and repeatability in analyzing inter-turn fault behavior. However, bench testing remains a necessary procedure for validating the accuracy and credibility of simulation models when feasible. Although this thesis focuses on simulation-based analysis, the use of experimental validation is still recommended for future research.

2.1 Stator Voltage Equation Based Modelling Approach

One fundamental approach to modeling an electric machine is through the use of stator winding voltage equations. This set of base equations consists of three expressions, each representing the voltage across the A, B, and C phase windings. Each equation includes both resistive and inductive components. The inductive terms also account for the back electromotive force (back EMF) generated by the rotating permanent magnets which differs depending on different PM machine structures such as SPMSM, IPMSM, or SynRM. This section summarizes few techniques derivate the mathematic governing relation for describing PMSM physics.

2.1.1 Space Vector Based Derivation Method

The formulation of the stator voltage equations can be derived using the space vector representation of the electric machine, as detailed in [39]. This approach summarizes the three-phase voltages, currents, or flux linkages into a single complex vector. In this representation (2.1), where $\boldsymbol{a} = e^{j\frac{2\pi}{3}}$ represents the three phase vectors are separated by 120° electrical degrees, the resulting space vector, denoted as $\boldsymbol{f_{abc}}$ stands for the net voltage, current, or flux vector rotating in the complex plane. Its magnitude and orientation vary dynamically based on the instantaneous values of the individual phase components

$$\boldsymbol{f_{abc}} \equiv \frac{2}{3}(f_a + \boldsymbol{a} f_b + \boldsymbol{a^2} f_c) \tag{2.1}$$

One of the key advantages of the space vector approach is that it eliminates the need to perform explicit reference frame transformations using matrix operations. The net voltage, current, or flux is represented as a single space vector within a stationary reference frame, where the three phase components are separated by 120° electrical degrees apart to reflect their positions in the *a-b-c* three-phase system.

$$\boldsymbol{f^e_{dqs}} = \boldsymbol{f_{abc}} e^{-j\omega_e t} \tag{2.2}$$

$$\boldsymbol{f^e_{dqr}} = \boldsymbol{f_{abcr}} e^{-j(\theta_e - \theta_r)} \tag{2.3}$$

This space vector can then be projected onto the stationary orthogonal *α-β* (also referred to as *d-qs* where s stands for stational) reference frame, and subsequently transformed into the rotating *d-q0* reference frame, which rotates with the machine synchronous frame. These transformations are performed using the Clarke and Park transformation matrices, or conveniently through exponential operator formulations in the complex domain (2.2), (2.3) as detailed in [5].

While the space vector-based derivation method offers analytical elegance and is convenient for hand calculations and theoretical analysis, it is less suitable for direct implementation in numerical software simulations due to its reliance on abstract vector formulations and rotational phasor representations.

2.1.2 Phase Variable Equivalent Circuit Based Derivation Method

Another common approach to developing the stator winding voltage model is to derive the voltage equations directly from the individual phase windings using Kirchhoff's Voltage Law (KVL) and magnetic coupling relationships, based on the machine's equivalent electrical circuit [6], [7]. This method results in a set of three coupled differential equations representing the voltages in phases A, B, and C. The derivation involves considering the resistive and inductive matrices and rotor back EMF matrix induced by the rotating permanent magnets. The resulting set of *a-b-c* reference frame equations is then transformed into the rotating *dq0* reference frame using the Clarke and Park transformation matrices, as described previously. This phase-variable approach is often employed to validate the space vector formulation, while *dq*-axis voltage equations are particularly well-suited for direct implementation in numerical software for machine control and dynamic simulation. This method is employed throughout the thesis, with further explanation provided in later sections.

2.2 State-space Representation of Stator Voltage Equation Based Model

While Stator voltage equation-based model offers a valuable method to simulate PMSM on numerical software, its state-space representation is generally preferred, and often necessary, for simulation and control system design. Most numerical solvers in software environments such

as MATLAB Simulink, PLECS, or Modelica prefer linear models and often provide tools to linearize nonlinear systems. Among these, the state-space representation is a widely adopted and well-supported approach for both analysis and controller design.

$$\dot{x} = \boldsymbol{A}x + \boldsymbol{B}u + \boldsymbol{f}$$
$$y = \boldsymbol{C}x + \boldsymbol{D}u \tag{2.4}$$

The standard state-space form is given as (2.4), where x is the system state vector, u is the input vector, and x represents the time derivative of the system states. The complete state-space model is defined by combining the system matrix $\boldsymbol{A}$, input matrix $\boldsymbol{B}$, output matrix $\boldsymbol{C}$, feedthrough matrix $\boldsymbol{D}$, and, where applicable, an offset vector $\boldsymbol{f}$.

From a control perspective, the permanent magnet (PM) machine is typically modeled as a nonlinear, multi-input multi-output (MIMO) system, due to its coupled electrical and mechanical dynamics, nonlinear back-EMF terms, and, in IPMSM cases, magnetic saliency. This nonlinearity and becomes even more pronounced when additional complexities are introduced, such as saliency effects in IPMSMs, faulted winding axis added, or machine is controlled and simulated under dynamic load conditions. Given these factors, modeling the stator voltage equations without adopting a state-space representation can lead to several issues. First, numerical instability may arise, often requiring smaller time steps or the use of stiff solvers, which significantly increases simulation time. Second, the model lacks a systematic framework, in other word, well structed system block, for defining system states and tracking inputs and outputs, making it prone to errors and difficult to maintain or scale. Finally, bypassing the state-space form limits compatibility with most linear control strategies, such as PID controllers. [8] introduces a method for modeling a SMPMSM with an inter-turn fault using state-space representation. The model is initially

developed in the *a-b-c* reference frame using stator voltage equations. The inter-turn fault is introduced by modifying the resistance and inductance matrices based on a shorted turn ratio $\mu = N_{sh}/N_s$ and a fictitious fault resistance R_f. After deriving the voltage and flux linkage equations for both the healthy and faulty windings, the model is transformed into the rotating dq reference frame using Clarke and Park transformations. The resulting equations are then expressed in a standard linear state-space form which enables efficient time-domain simulation. Although the results in [8] are based on a steady-state configuration, the state-space representation of the stator voltage equation-based model, enabled by its linear structure, can be readily integrated into a closed-loop system for dynamic performance analysis and controller design studies.

It is important to note that the state-space representation of the stator voltage equation-based model has several limitations. First, its linear approximation may fail to capture system behavior under highly nonlinear conditions, such as inverter switching signals, machine saliency, or magnetic saturation, resulting in reduced accuracy. Second, for stiff systems, careful selection of numerical solvers and smaller time steps is required to maintain stability; otherwise, the simulation may become numerically unstable. Finally, the complexity involved in constructing the state-space model makes it less convenient for tuning machine parameters in repetitive simulations. Due to these limitations, the state-space representation is not an ideal candidate for training machine learning models for inter-turn fault detection.

2.3 Flux Linkage Based Magnetic Domain Model

Another common approach to modeling a PM machine is to utilize the stator-rotor flux linkage directly, rather than formulating voltage equations as discussed in Chapter 2.1. Several numerical simulation platforms, such as the Simulink-Simscape environment, PLECS, or PSIM

with its control suite add-on, support the integration of magnetic and electrical circuit components alongside numerical method-based control systems. This allows for the construction of machine models in the magnetic domain using physically meaningful components to intuitively represent the machine's structure and magnetic flux paths as illustrated in (Figure 2.1), and followed by implementing the control strategies.

The key challenge to construct flux linkage based Magnetic domain model is modeling the stator-rotor air gap and magnetically coupled rotor. Unlike the stationary winding components, the rotor in a PM machine is a mechanically rotating part for which the mechanical-magnetic coupled relationship needs to be represented. To address this, depending on the software used, it is necessary to introduce the rotor position angle into the flux linkage, either through a custom coding block or a user-defined rotor component, for example the custom defined rotor Simscape component block as (Figure 2.1) shown.

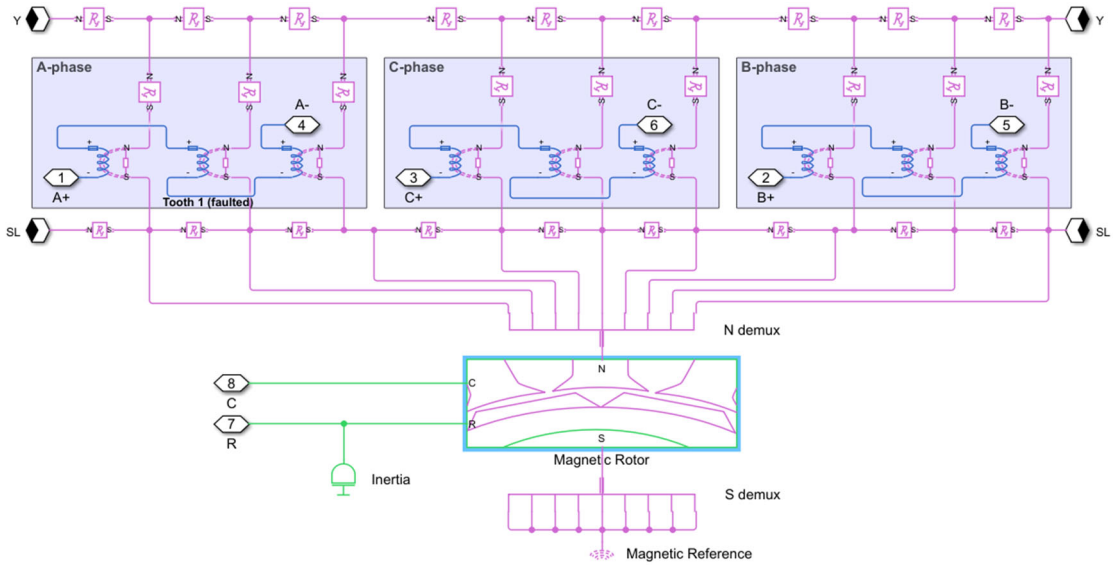

Figure 2.1 Simscape PMSM magnetic domain model [9].

One of the key benefits of using a magnetic domain model lies in the physical interpretability of each component, notably the winding coils, magnetic reluctances, and magnetomotive force (MMF) sources. This modeling approach enables highly localized fault representation at the winding level, with the flexibility to tune parameters at the component level. Such granularity allows the simulation results to capture subtle distinctions between various fault types and locations with improved precision. Furthermore, this approach supports the incorporation of non-ideal magnetic materials, making it possible to represent the coupled electromagnetic–mechanical interactions arising from magnetic saturation and material nonlinearity under inter-turn short-circuit fault conditions.

Despite its benefits, the flux linkage-based magnetic domain model is associated with notable drawbacks. The increased computational complexity results in a model lack of analytical simplicity which diminishes model's repeatability for machine learning model training purpose. Additionally, this type of magnetic domain models exhibits nonlinear characteristics, which often pose challenges when integrated with linear controllers and consequently restricts its applicability in control-oriented simulations.

2.4 Final Element Method (FEM) Based Model

As an extension of the flux linkage-based magnetic domain modeling approach, a finite element method (FEM) mesh can be generated from a PM machine's CAD geometry, whether in two or three dimensions, and coupled with an equivalent circuit model to capture the machine's electromagnetic behavior (Figure 2.2). This FEM-based model enables high-resolution visualization of flux density and current distribution from both 2D and 3D perspectives, offering improved accuracy compared to the previously discussed methods, depending on the mesh and

solver settings, in addition non-ideal permeability and magnetic non-linearity can be considered in these types of models. The structural complexity associated with modeling the mechanically rotating rotor in conjunction with the stationary stator and intervening air gap can be addressed through advanced FEM software features and appropriate meshing techniques. However, the detailed implementation of such methods lies beyond the scope of this thesis.

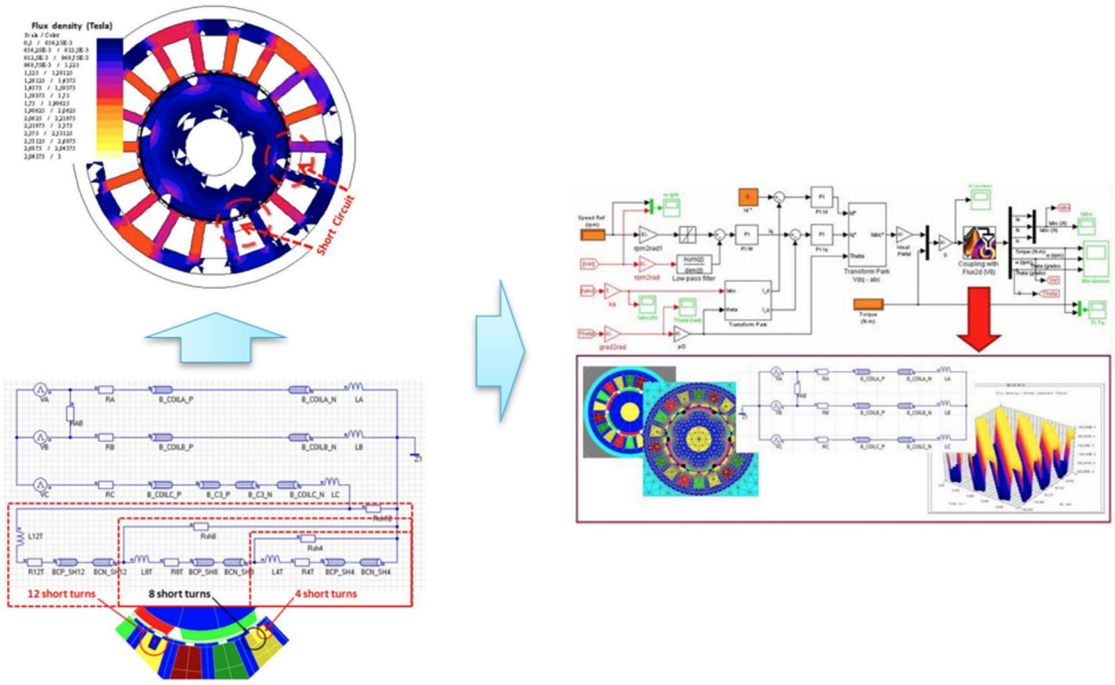

Figure 2.2 Representation of FEM modeling approach for PMSM [10].

Although this model exhibits similar control-oriented drivability to the previously discussed flux linkage-based magnetic domain model, it is fundamentally underlain by an equivalent circuit representation. The improved accuracy achieved through this approach, however, comes at the expense of higher computational cost. Another major drawback of both the FEM-based model and the flux linkage based magnetic domain model is the tedious process of parameter

tuning, which stems from their reliance on detailed physical representations. These factors are misaligned with the objectives of training a machine learning model for inter-turn fault detection, which relies not only on model accuracy and total simulation runtime, but also, most importantly, on the scalability of the model. To generate sufficient and diverse training data, models with varying parameters must be simulated efficiently.

Chapter 3
Overview of Phase Winding Inter-turn Short Fault Detection Techniques

Extensive research has been conducted on online detection methods for stator turn faults in PMSMs [11] – [15], where the term "online" refers to the capability of detecting faults while the machine is in operation. Some of these approaches remain at the simulation level, where the machine is typically driven by idealized sinusoidal three-phase voltage sources, without incorporating the effects of gate-level pulse-width modulation (PWM) control signals or closed-loop control strategies. This simplification is often adopted due to the inherent complexity of accurately modeling fault behavior, as discussed in Chapter 2. Alternatively, other studies are conducted on bench test platforms, where actual phase-to-neutral currents or voltages are measured and fault signatures are extracted using various signal processing techniques.

This chapter presents a summary of commonly used fault indicators for inter-turn fault detection in PM machines, along with a review of selected online detection techniques across literatures.

3.1 Symmetrical Components

The method of symmetrical components is a mathematical framework used to analyze three-phase systems especially unbalanced system through decoupled phasor representations. This method not only ease the study of three-phase systems but is particularly valuable in diagnosing asymmetries arising from fault conditions. Any arbitrary three-phase system can be decomposed into three sets of balanced phasors known as the positive-sequence, negative-sequence, and zero-sequence components as illustrated in (Figure 3.1).

- The positive-sequence component consists of three phasors that are equal in magnitude, separated by 120 electrical degrees, and follow the phase sequence A–B–C.
- The negative-sequence component also comprises three phasors equal in magnitude and 120 degrees apart, but with the reversed phase sequence C–B–A.

- The zero-sequence component consists of three identical phasors that are equal in both magnitude and phase angle, exhibiting no phase displacement among them.

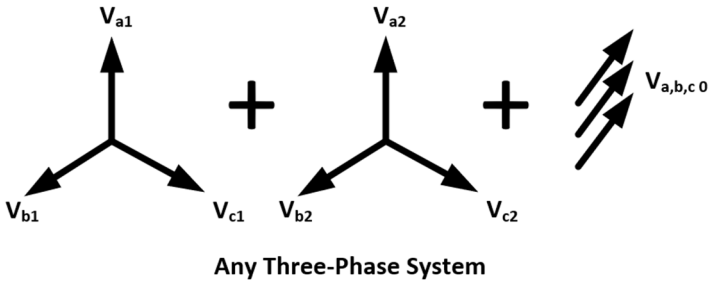

Figure 3.1 Decomposition of three-phase system into symmetrical components.

Symmetrical component analysis can be applied to any three-phase quantity, such as voltage, current, flux, or impedance. The mathematical representation of symmetrical components can be derived by defining the variable notations as shown in (Figure 3.2), where “V” denotes voltage, the subscript “b” indicates phase b, and the subscript “2” represents the negative-sequence component.

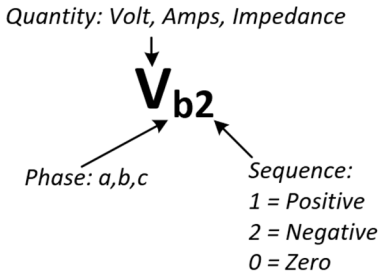

Figure 3.2 Notation convention for symmetrical component quantities.

Since each phase quantity is the vector sum of its corresponding positive-, negative-, and zero-sequence components, the phase voltages V_a, V_b, V_c can be expressed accordingly, as shown in (3.1)[16]

$$V_A = V_{A0} + V_{A1} + V_{A2}$$

$$V_B = V_{B0} + V_{B1} + V_{B2} \tag{3.1}$$

$$V_C = V_{C0} + V_{C1} + V_{C2}$$

These expressions can be further simplified by introducing the complex operator $\boldsymbol{a} = e^{j\frac{2\pi}{3}}$, which represents a 120° degree phase shift, and applying the appropriate substitutions, as illustrated in the matrix form:

$$\begin{vmatrix} V_A \\ V_B \\ V_C \end{vmatrix} = \begin{vmatrix} 1 & 1 & 1 \\ 1 & a^2 & a \\ 1 & a & a^2 \end{vmatrix} \times \begin{vmatrix} V_{A0} \\ V_{A1} \\ V_{A2} \end{vmatrix} \tag{3.2}$$

Solving for the sequence components yields:

$$\begin{vmatrix} V_{A0} \\ V_{A1} \\ V_{A2} \end{vmatrix} = \frac{1}{3}\begin{vmatrix} 1 & 1 & 1 \\ 1 & a^2 & a \\ 1 & a & a^2 \end{vmatrix} \times \begin{vmatrix} V_A \\ V_B \\ V_C \end{vmatrix} \tag{3.3}$$

(3.2) and (3.3) thus serve as transformation matrices that enable conversion between phase quantities from symmetrical components or vice versa. Given these mathematical relations, any arbitrary three-phase systems can be decoupled into a set of positive-, negative-, and zero-sequence components.

An ideal balanced three-phase system contains only the positive-sequence component, such as positive-sequence voltage, due to the alignment in magnitude, phase displacement, and

sequence between the positive-sequence component and a perfectly balanced three-phase system. As a result, the negative- and zero-sequence voltage components are identically zero. However, when any form of imbalance is introduced into the system, these components become nonzero, in accordance with the principle of vector superposition.

3.2 Fault Indicators

In most traction applications, machines are driven by CCVSIs, where the inverter actively adjusts its three-phase voltage output to regulate the machine's current draw based on a PI, field-oriented (FOC) or other control loop. Given that the current is continuously maintained within desired limits by the CCVSI, the presence of an inter-turn fault may not produce clear or significant signatures in the measured current. Therefore, effective turn fault detection requires hard indicators that are highly sensitive to such faults while being independent to the controller’s compensating actions.

However, those hard indicators are only used under simulation or bench-testing environments, for validation of current-based fault detection result, as they often rely on measuring the neutral point voltage of the three-phase winding, which is difficult to access or define precisely in practice. For online fault detection in electric vehicle (EV) applications, the diagnostic method must rely solely on current sensing, as most traction inverters are equipped only with high-accuracy current sensors for control purpose. The addition of a high-resolution three-phase voltage sensing interface is typically infeasible due to cost, packaging and EMC constraints.

3.2.1 Fundamental Negative Sequence Voltage

A stator inter-turn fault in an otherwise balanced three-phase PMSM results in an electrical imbalance within the system. As discussed in Section 3.1, this imbalance gives rise to a fundamental negative-sequence component in the stator line-to-neutral voltages and line currents [17]. In response, the traction CCVSI continuously adjusts its line-to-neutral voltage output to regulate the three-phase line currents, ensuring they track their reference values to maintain the desired torque output. Throughout this process, no negative-sequence component current will be observed assuming perfect current reference and controller, but fundamental negative-sequence component will appear on the CCVSI line-neutral voltage output, because CCVSI injects the necessary negative-sequence voltage to maintain symmetry of the current regulation. While this holds true under ideal conditions, in practical applications the line-to-neutral voltage output of a CCVSI often exhibits slight imbalances even in the absence of stator turn faults. These deviations can arise from various factors, including DC bus voltage ripple, non-idealities in PWM due to semiconductor characteristics, sensor errors, and the finite bandwidth of the control system.

PMSM's rotor speed (position) is used as one of feed-back-input of machine controller. This speed (position) sensing signal is critical for transforming the three-phase output currents of the VCCSI from the stationary *a-b-c* reference frame to *dq* reference frame rotating with machine's synchronous frame for flux and torque control. Additionally, the same feedback signal is used to inverse-transform the *dq* current commands and reference back into the stationary $\alpha\beta$ reference frame, allowing the PWM module to generate appropriate voltage control signals. Under stator winding inter-turn fault condition, this speed (position) feedback signal contains second order harmonic. If not properly filtered, this harmonic can distort the symmetry of current reference frame and lead to the appearance of negative-sequence component in the line currents.

Consequently, in real-world application, negative-sequence component is typically observed in both the VCCSI line-to-neutral voltage output and the PM machine's three-phase line currents. Various fault detection methods based on negative-sequence components have been proposed in the literature [18]-[22].

3.2.2 Fundamental Zero Sequence Voltage

When a PM machine experiences a stator winding inter-turn short, phase impedance asymmetry is introduced. This asymmetry can induce a fundamental zero-sequence voltage component in PM machines with wye-connected windings. Related fault detection methods based on this phenomenon have been proposed in the literature [23]-[28]. In a wye-connected three-phase winding, the sum of the line-to-neutral voltages of all three phases is given by:

$$\tilde{V}_{sum} = \tilde{V}_{an} + \tilde{V}_{bn} + \tilde{V}_{cn} = Z_a\tilde{I}_a + Z_b\tilde{I}_b + Z_c\tilde{I}_c \tag{3.4}$$

Here, Z and I denote the phase winding line impedance and current, respectively. The subscripts a, b, and c indicate the corresponding phases, while the subscript n refers to the floating neutral point of the wye-connected winding. For a machine with symmetrical windings, the three-phase impedance is given by:

$$Z_a = Z_b = Z_c \tag{3.5}$$

Additionally, in a wye-connected winding configuration, Kirchhoff's Current Law (KCL) dictates that the sum of the phase currents must be zero, as expressed in (3.6).

$$\tilde{I}_a + \tilde{I}_b + \tilde{I}_c = 0 \tag{3.6}$$

Equations (3.4), (3.5), and (3.6) show that the sum of the phase line-to-neutral voltages in a perfectly symmetric PMSM is zero. This implies that the floating neutral point of the machine's

wye-connected winding remains at the same potential as the DC bus ground of the VCCSI. Conversely, if any fault, whether an inter-turn short or a phase-to-phase short, occurs within the wye-connected winding, the voltage relationship is no longer valid. As a result, the sum of the phase line-to-neutral voltages becomes nonzero, giving rise to fundamental zero-sequence voltage component in the system.

The zero-sequence voltage component is a highly accurate indicator for detecting stator winding short faults, owing to its inherent independence from controller actions. However, this indictor is limited to wye-connected windings and, as previously discussed, locating and accessing the stator winding neutral point is often challenging. Therefore, this zero-sequence voltage component is typically employed to validate results obtained from other online detection methods on simulation level.

3.2.3 Second Order Harmonic in the d-axis Current

Despite advanced control strategies such as Maximum Torque per Ampere (MTPA) and flux weakening, the *dq*-axis current components, which rotate with the machine's synchronous reference frame, are typically considered constant under steady-state conditions. This feature enables more effective fault identification compared to using the stationary three-phase currents, which are represented as sinusoidal waveforms. As detailed in Chapter 3.2.1, In a CCVSI-driven machine, a stator turn fault induces a negative-sequence current, which manifests as a second-order harmonic component in the synchronously rotating *dq*-reference frame. both *d*-axis current I_d and *q*-axis current I_q are influenced by this harmonic.

In a typical scenario, regardless of PM machine type, the *q*-axis current component provides the speed (position) and torque reference to the machine controller and varies according

to the given speed (position) and torque command. In contrast, the *d*-axis current component provides the flux reference, which becomes relevant primarily when saliency, MTPA, or flux weakening control is applied. For the control of a healthy SPMSM, the *d*-axis current reference is typically maintained at zero. During dynamic operation, I_q varies continuously in response to changing torque commands, making it more difficult to distinguish fault-related harmonics from normal control-induced variations. Consequently, monitoring second-order harmonics in Id, relative to its nominal control value, provides a more reliable indicator of inter-turn faults in CCVSI-controlled machines as it is more independent of controller actions.

The advantage of using d-axis current as a fault indicator is primarily limited to SPMSM applications. In IPMSMs, its *d*-axis current stays within a preset relation with *q*-axis current depend on torque command. As result, its independence from the controller vanishes.

3.2.4 Second Order Harmonic in the Three-phase Current

The stationary *abc*-reference frame phase currents are typically not considered ideal for fault indication due to their fundamental sinusoidal profile. In most cases, higher-order harmonics must be monitored to enable effective fault detection. Nevertheless, this fault indicator can still be useful in certain scenarios, such as in machine learning-based fault diagnosis, where cross-verification using multiple fault indicators is employed to improve the accuracy of the trained model.

Following the same principle of fault indication using *dq*-axis currents discussed in Chapter 3.1.3, controller-induced interference causes negative-sequence components to be distributed across all phases of the *abc*-phase currents. A signal-to-signal Fourier analysis must therefore be performed to compare the spectral content of a controlled, healthy PM machine against that of a

machine with inter-turn short faults. Due to errors and variations introduced from other sources in practical applications, second- and higher-order harmonic components must be analyzed to accurately assess the presence of inter-turn short faults

Harmonic analysis of the *abc*-phase currents, when combined with other robust fault indicators, provides an alternative feature set for training machine learning-based fault detection models. This approach further enhances the accuracy of the trained fault detection model.

3.3 Signal Processing Techniques for Fault Detection

For processing non-stationary signals, two widely used techniques are introduced in this chapter: Short-Time Fourier Transform (STFT) and Wavelet Transform (WT). Both techniques are particularly effective in analyzing signals whose frequency content varies over time, which is a common characteristic in electrical machines, especially under fault conditions. These techniques are frequently applied to extract and analyze harmonic spectra within the stator current components, which are critical to trigger stator winding inter-turn short circuits fault indicators listed in chapter 3.2.

The STFT provides a time-frequency representation suitable for tracking gradual changes in harmonic patterns but is limited in detecting fast transients. In contrast, the WT offers adaptive resolution, making it more effective for capturing localized, transient disturbances associated with fault initiation and dynamic operating conditions.

Together, these two complementary techniques provide a powerful toolkit for analyzing the dynamic behavior of stator inter-turn fault signal and enhancing the sensitivity and robustness of fault detection in permanent magnet machines.

3.3.1 Short Time Fourier Transformation (STFT) Turn Fault Detection

Across reviewed literature, inter-turn short fault detection typically involves analyzing abnormal higher-order harmonic components in currents using the Short-Time Fourier Transform (STFT).

The STFT is the standard method analyze the frequency content of a signal change over time. Fourier transform is applied to short, overlapping segment of time window of the signal. Energy distribution of the different frequency component is then calculated refer to the center of each time window just like traditional Fourier transform [29]

The STFT of a continuous-time signal x(t) is defined as (3.7), where w(t) is the time window function centered at time τ , so called time-shift parameter.

$$STFT(\tau, f) = \int_{-\infty}^{\infty} x(t)w(t-\tau)e^{-j2\pi ft}\, dt \tag{3.7}$$

The STFT offers several advantages over the traditional Fourier Transform when analyzing non-stationary signals whose frequency content changes over time. In STFT, a longer time window results in better frequency resolution, that is, it improves the ability to distinguish between closely spaced frequency components. However, a major drawback is that it also reduces time resolution, making it harder to determine when those frequency components occur in the time domain. This limitation becomes critical when analyzing PM machines operating under dynamic load transitions. During such transitions, the frequency content of the signal can change abruptly. If an inappropriate time window is selected, it may either obscure the timing of fault-related frequency components or fail to resolve them accurately due to poor frequency resolution. As a result, faults may go undetected or be misidentified when compared against preset fault detection algorithms.

3.3.2 Wavelet Transformation (WT) Turn Fault Detection

Similar to STFT, Wavelet Transform (WT) is another technique used to analyze fault-related harmonic components in phase currents (A, B, and C). To address the time–frequency resolution trade-off inherent in STFT, the WT was developed. Unlike STFT, which uses a fixed window size across all frequencies, the WT adapts flexible time window length, that is shorter windows for high-frequency components and longer windows for low-frequency components. This makes WT particularly better-suited for analyzing non-stationary signals with time-varying frequency content [30]. The continuous Wavelet Transform (CWT) of a signal is given by (3.8), where a is scale (frequency) parameter and τ is time parameter.

$$CWT(a,\tau) = \frac{1}{\sqrt{a}} \int_{-\infty}^{+\infty} x(t)\ g\left(\frac{t-\tau}{a}\right) dt \tag{3.8}$$

The scalogram of WT, which is a 2D time-frequency plot and use color to display energy of different frequencies (scales) change over time, can be obtained by taking the squared modulus of CWT as:

$$Scalogram(a,\tau) = |CWT(a,\tau)|^2 \tag{3.9}$$

One limitation of the Wavelet Transform (WT) is that its performance heavily depends on the choice of the mother wavelet *g(t)* in the transform equation, where $\frac{t-\tau}{a}$ represents the scaling and shifting of the wavelet. There is no universal wavelet that works best for all types of signals. Additionally, the selected wavelet must satisfy a mathematical condition known as the admissibility condition, which requires the wavelet to be localized in time and have a zero average (3.10). This condition ensures that the wavelet behaves like a band-pass filter, enabling it to effectively detect changes and transient features in the signal.

$$\int_{-\infty}^{\infty} g(t)\ dt = 0 \tag{3.10}$$

Due to its limitations, the Wavelet Transform (WT) is not a perfect candidate for processing fault current signals and performing online detection in PM machines. Unpredictable load changes and transients can lead to missed detections or false alarms, reducing the reliability of the method.

Chapter 4
PMSM Theoretical Framework

As outlined in Section 2.1, the most fundamental way to simulate a PMSM is to begin with its phase-variable equivalent circuit and formulate the stator-voltage equations. When the machine is healthy, the three-phase model can be transformed into the *d-q* reference frame, yielding a compact two-state description that is both numerically efficient and sufficiently accurate, if the model is properly constructed.

Modelling a stator inter-turn short circuit, however, poses additional challenges. The faulted turn must remain in the *a-b-c* frame so that its voltage drops, circulating current and mutual inductances are represented explicitly. Consequently, the original 3×3 inductance- and resistance-matrix pair is expanded to a 4×4 formulation, and an extra state equation is introduced for representing fault-loop current and voltage relationship. This higher-order system is considerably stiffer than the healthy model and gives rise to algebraic loops when implemented in ODE/DAE-solver-based environments such as Simulink or PLECS. If the algebraic loop is broken by inserting a Unit Delay block, the resulting one-sample latency alters the closed-loop dynamics; in fast or lightly-damped loops this additional phase lag can degrade accuracy or lead to instability [31], in severe cases, precipitate solver divergence. Robust simulation therefore demands either an implicit DAE solver capable of resolving the algebraic constraints iteratively, or an analytical reformulation that renders the state vector explicit without resorting to discrete delays.

To address these challenges, Chapter 4 introduces a novel modelling framework for PMSMs affected by stator inter-turn faults. The equation-based fault dynamics are encapsulated in a custom Simscape component (.ssc file), where its acausal syntax and implicit DAE solver automatically resolve the expanded system of differential- and algebraic-equations, eliminating the need for artificial delays or manual equation rearrangement. The resulting block drops directly

into a standard Simulink diagram, where it interfaces seamlessly with the closed-loop controller, enabling fast and numerically robust time-domain simulation of the inter-turn faulted PMSM.

4.1 Governing Voltage Equations of SPMSM Stator Windings

This chapter establishes the analytical foundation for developing custom Simscape components for both SPMSM and IPMSM. Based on equivalent circuit theory, the stator winding voltage equations are formulated in the three-phase reference frame, with particular attention to the development of resistance and inductance matrices that account for inter-turn short circuits. These three-phase equations are subsequently transformed into the *dq*-axis for control applications. Furthermore, the torque equation is derived for both faulted SPMSM and IPMSM, facilitating subsequent torque control strategies.

For clarity, the subscripts used in Section 4.1 are defined as follows: $\boldsymbol{s}$ denotes SPMSM, $\boldsymbol{i}$ denotes IPMSM, $\boldsymbol{h}$ denotes the healthy machine, and $\boldsymbol{f}$ denotes the stator winding inter-turn short-circuited machine.

4.1.1 Healthy SPMSM Governing Voltage Equations

The standard equations for SPMSM in *abc* reference frame are given below:

$$\left[\boldsymbol{V_{sh,abc}}\right] = \left[\boldsymbol{R_{sh,abc}}\right] \cdot \left[\boldsymbol{I_{sh,abc}}\right] + \frac{d}{dt}\left[\boldsymbol{\lambda_{sh,abc}}\right] \tag{4.1}$$

Where the phase voltage and current can be expressed into vector form as (4.2) (4.3)

$$[\boldsymbol{V_{sh,abc}}] = \begin{bmatrix} v_a \\ v_b \\ v_c \end{bmatrix} \tag{4.2}$$

$$[\boldsymbol{I_{sh,abc}}] = \begin{bmatrix} i_a \\ i_b \\ i_c \end{bmatrix} \tag{4.3}$$

Assuming infinite permeability and a linear magnet, the stator flux component $\lambda_{s,abc}$ can be written as the sum of two contributions as (4.4): the flux linkage produced by the stator windings and the flux provided by the rotor's permanent magnets.

$$[\boldsymbol{\lambda_{sh,abc}}] = [\boldsymbol{L_{sh,abc}}] \cdot [\boldsymbol{I_{sh,abc}}] + [\boldsymbol{\lambda_{PM,abc}}] \tag{4.4}$$

Accordingly, the resistance and inductance matrices are given by (4.5) and (4.6), respectively.

$$[\boldsymbol{R_{sh,abc}}] = \begin{bmatrix} R_s & 0 & 0 \\ 0 & R_s & 0 \\ 0 & 0 & R_s \end{bmatrix} \tag{4.5}$$

$$[\boldsymbol{L_{sh,abc}}] = \begin{bmatrix} L & M & M \\ M & L & M \\ M & M & L \end{bmatrix} \tag{4.6}$$

In the *abc* reference frame, the flux linkage produced by the rotor's permanent magnets is given in (4.4), with only the fundamental harmonic component considered. The constant λ_{PM} is a machine parameter which denotes the peak flux linkage contributed by the permanent magnets. The electrical angle is defined as $\theta_e = p\theta_m$, where p is the number of pole pairs and θ_m is the mechanical rotor angle.

$$[\boldsymbol{\lambda_{PM,abc}}] = \lambda_{PM} \begin{bmatrix} cos\,\theta \\ cos(\theta - 2\pi/3) \\ cos(\theta + 2\pi/3) \end{bmatrix} \tag{4.7}$$

From equation (4.1) to (4.4), the general representation of healthy SPMSM in *abc* reference frame is given by (4.8)

$$[\boldsymbol{V_{sh,abc}}] = [\boldsymbol{R_{sh,abc}}] \cdot [\boldsymbol{I_{sh,abc}}] + [\boldsymbol{L_{sh,abc}}] \cdot \frac{d}{dt}[\boldsymbol{I_{sh,abc}}] + \frac{d}{dt}[\boldsymbol{\lambda_{PM,abc}}] \tag{4.8}$$

The standard Park transformation that maps variables from the stationary *abc*-reference frame to the rotating *dq* reference frame is given in (4.9) expressed by $\boldsymbol{T}$, where the third row represents the zero-sequence component defined in Chapter 3.2.2.

$$[\boldsymbol{T}] = \begin{bmatrix} d \\ q \\ 0 \end{bmatrix} = \frac{2}{3}\begin{bmatrix} cos\,\theta & cos(\theta - 2\pi/3) & cos(\theta + 2\pi/3) \\ -sin\,\theta & -sin(\theta - 2\pi/3) & -sin\,\theta(\theta + 2\pi/3) \\ 1/2 & 1/2 & 1/2 \end{bmatrix}\begin{bmatrix} a \\ b \\ c \end{bmatrix} \tag{4.9}$$

Applying the transformation to both side of the equation (4.8), and replace the current vector in *abc*-reference frame with $\boldsymbol{T^{-1}} \cdot [\boldsymbol{I_{sh,dq0}}]$ where $\boldsymbol{T^{-1}}$ denotes the inverse Park transformation., as. Recall that whenever $\boldsymbol{T}$ or $\boldsymbol{T^{-1}}$ is time-differentiated and the derivative must be evaluated with the product rule while multiplied by another time-varying matrix.

$$\begin{aligned}[\boldsymbol{V_{sh,dq0}}] = \boldsymbol{T}[\boldsymbol{R_{sh,abc}}] \cdot \boldsymbol{T^{-1}} \cdot [\boldsymbol{I_{sh,dq0}}] + \boldsymbol{T} \cdot [\boldsymbol{L_{sh,abc}}] \cdot \frac{d\boldsymbol{T^{-1}}}{dt}[\boldsymbol{I_{sh,dq0}}] \\ + \boldsymbol{T} \cdot [\boldsymbol{L_{sh,abc}}] \cdot \boldsymbol{T^{-1}} \cdot \frac{d[\boldsymbol{I_{sh,dq0}}]}{dt} + \boldsymbol{T} \cdot \frac{d\boldsymbol{T^{-1}}}{dt} \cdot [\boldsymbol{\lambda_{PM,dq0}}] \\ + \boldsymbol{T} \cdot \boldsymbol{T^{-1}} \cdot \frac{d[\boldsymbol{\lambda_{PM,dq0}}]}{dt}\end{aligned} \tag{4.10}$$

This operation produces the standard *dq*-axis stator-voltage model for a SPMSM, shown below (4.11) - (4.13). For a perfectly balanced machine the zero-sequence voltage term vanishes.

Moreover, because a SPMSM exhibits no salient poles, the stator inductance is isotropic, thus $L_s = L_d = L_q = \mathrm{L} - M$.

$$\textit{d-axis voltage equation:} \quad v_d = r_s i_d + L_s \frac{di_d}{dt} - \omega_e L_s i_q \tag{4.11}$$

$$\textit{q-axis voltage equation:} \quad v_q = r_s i_q + L_s \frac{di_q}{dt} + \omega_e L_s i_d + \omega_e \lambda_{PM} \tag{4.12}$$

$$\textit{Zero-sequence voltage equation:} \quad v_0 = \frac{1}{3} v_a + \frac{1}{3} v_b + \frac{1}{3} v_c = 0 \tag{4.13}$$

4.1.2 Healthy IPMSM Governing Voltage Equations

Rephrasing the base wind equation in *abc*-reference frame (4.14) which applies for both SPMSM and IPMSM. With $\left[\boldsymbol{V_{ih,abc}}\right] = [v_a \quad v_b \quad v_c]^T$ and $\left[\boldsymbol{I_{ih,abc}}\right] = [i_a \quad i_b \quad i_c]^T$

$$\left[\boldsymbol{V_{ih,abc}}\right] = \left[\boldsymbol{R_{ih,abc}}\right] \cdot \left[\boldsymbol{I_{ih,abc}}\right] + \frac{d}{dt}\left[\boldsymbol{\lambda_{ih,abc}}\right] \tag{4.14}$$

Under the same assumption of infinite permeability and magnet linearity, $\left[\boldsymbol{\lambda_{ih,abc}}\right]$ is decomposed into the sum of the flux linkage produced by the stator windings and rotor's permanent magnets. The difference is the stator winding inductance matrix is rotor electrical angle position dependent, which is expressed by $\boldsymbol{L_{ih,abc}}(\theta)$.

$$\left[\boldsymbol{\lambda_{ih,abc}}\right] = \left[\boldsymbol{L_{ih,abc}}(\theta)\right] \cdot \left[\boldsymbol{I_{ih,abc}}\right] + \left[\boldsymbol{\lambda_{PM,abc}}\right] \tag{4.15}$$

The general stator winding voltage formulation for IPMSM is obtained by combining (4.14) and (4.15) and differentiating the flux term, while considering the inductance matrix's dependence on the electrical rotor angle

$$\begin{aligned}\left[\boldsymbol{V_{ih,abc}}\right] = \left[\boldsymbol{R_{ih,abc}}\right]\left[\boldsymbol{I_{ih,abc}}\right] + \left[\boldsymbol{L_{ih,abc}}(\theta)\right]\frac{d\left[\boldsymbol{I_{ih,abc}}\right]}{dt} \\ + \frac{d\left[\boldsymbol{L_{ih,abc}}(\theta)\right]}{dt}\left[\boldsymbol{I_{ih,abc}}\right] + \frac{d\left[\boldsymbol{\lambda_{PM,abc}}\right]}{dt}\end{aligned} \tag{4.16}$$

Which is often written as (4.17) in order to emphasize is angle dependency for derivative terms depends on rotor angles, with ω_e denotes the rotor's synchronous frequency in electrical radians per second.

$$\begin{aligned}\left[\boldsymbol{V_{ih,abc}}\right] = \left[\boldsymbol{R_{ih,abc}}\right]\left[\boldsymbol{I_{ih,abc}}\right] + \left[\boldsymbol{L_{ih,abc}}(\theta)\right]\frac{d\left[\boldsymbol{I_{ih,abc}}\right]}{dt} \\ + \omega_e\frac{d\left[\boldsymbol{L_{ih,abc}}(\theta)\right]}{d\theta}\left[\boldsymbol{I_{ih,abc}}\right] + \omega_e\frac{d\left[\boldsymbol{\lambda_{PM,abc}}\right]}{d\theta}\end{aligned} \tag{4.17}$$

The resistance and inductance matrix $\boldsymbol{R_{ih,abc}}$ and $\boldsymbol{L_{ih,abc}}(\theta)$ can be expressed by following:

$$\left[\boldsymbol{R_{ih,abc}}\right] = \begin{bmatrix} R_i & 0 & 0 \\ 0 & R_i & 0 \\ 0 & 0 & R_i \end{bmatrix} \tag{4.18}$$

$$\left[\boldsymbol{L_{ih,abc}}(\theta)\right] = \begin{bmatrix} L_{aa}(\theta) & L_{ab}(\theta) & L_{ac}(\theta) \\ L_{ab}(\theta) & L_{bb}(\theta) & L_{bc}(\theta) \\ L_{ac}(\theta) & L_{bc}(\theta) & L_{cc}(\theta) \end{bmatrix} \tag{4.19}$$

From the inductance matrix, the general form of rotor-angle-dependent self- and mutual-inductances can be expressed as follows, explicitly accounting for higher-order spatial harmonics [32].

$$\begin{bmatrix} L_{aa}(\theta) \\ L_{bb}(\theta) \\ L_{cc}(\theta) \end{bmatrix} = \begin{bmatrix} L_{ls} + L_1 - \sum_{k=1}^{\infty} L_{2k} \cos(2k\theta) \\ L_{ls} + L_1 - \sum_{k=1}^{\infty} L_{2k} \cos[2k(\theta - 2\pi/3)] \\ L_{ls} + L_1 - \sum_{k=1}^{\infty} L_{2k} \cos[2k(\theta + 2\pi/3)] \end{bmatrix} \tag{4.20}$$

$$\begin{bmatrix} L_{ab}(\theta) \\ L_{bc}(\theta) \\ L_{ac}(\theta) \end{bmatrix} = \begin{bmatrix} -\frac{1}{2} L_1 - \sum_{k=1}^{\infty} L_{2k} \cos[2k(\theta - \pi/3)] \\ -\frac{1}{2} L_1 - \sum_{k=1}^{\infty} L_{2k} \cos[2k(\theta + \pi)] \\ -\frac{1}{2} L_1 - \sum_{k=1}^{\infty} L_{2k} \cos[2k(\theta + \pi/3)] \end{bmatrix} \tag{4.21}$$

Similarly, the general form of the flux linkage produced by the rotor's permanent magnets is given in (4.22), which can be further reduce to (4.23) if only the fundamental harmonic is considered.

$$\left[\boldsymbol{\lambda}_{\mathbf{PM},abc}\right] = \sum_{k=1}^{\infty} \lambda_{\text{PM 2k-1}} \begin{bmatrix} \sin[(2k-1)\theta] \\ \sin[(2k-1)(\theta - 2\pi/3)] \\ \sin[(2k-1)(\theta + 2\pi/3)] \end{bmatrix} \tag{4.22}$$

$$\left[\boldsymbol{\lambda}_{\mathbf{PM},abc}\right] = \lambda_{\text{PM}} \begin{bmatrix} \cos\theta \\ \cos(\theta - 2\pi/3) \\ \cos(\theta + 2\pi/3) \end{bmatrix} \tag{4.23}$$

By applying the Park transformation to the general form of the rotor-angle-dependent self- and mutual-inductance matrix (4.19), the cosine terms that describe angle-dependent inductances in the stationary reference frame are mathematically eliminated. This results in a pair of constant

inductances in the dq-reference frame, denoted as L_d and L_q. Applying the Park transformation to equation (4.16), following the same procedure used for the SPMSM, yields the dq-axis stator voltage expressions shown below:

$$\textit{d-axis voltage equation:} \quad v_d = r_s i_d + L_d \frac{di_d}{dt} - \omega_e L_q i_q \tag{4.24}$$

$$\textit{q-axis voltage equation:} \quad v_q = r_s i_q + L_q \frac{di_q}{dt} + \omega_e L_d i_d + \omega_e \lambda_{PM} \tag{4.25}$$

$$\textit{Zero-sequence voltage equation:} \quad v_0 = \frac{1}{3} v_a + \frac{1}{3} v_b + \frac{1}{3} v_c = 0 \tag{4.26}$$

While the fundamental form of the dq-axis voltage equations is consistent for IPMSM and SPMSM, the inherent machine property of rotor saliency dictates whether L_d and L_q are considered equal or unequal, leading to distinct operational characteristics and control strategies for IPMSMs compared to SPMSMs.

4.1.3 Inter-turn Short Fault SPMSM Governing Voltage Equations

For a SPMSM with an inter-turn short in the phase-a a stator winding, the equivalent circuit is shown in (Figure 4.1). The phase-a coil originally comprises N series turns, of which n turns are bypassed by a fault resistance R_f connected in parallel, representing the short-path impedance. The current i_f flowing through R_f is the circulating short-circuit current within the faulted coil segment. The short turn ratio is defined by $\mu = n/N$.

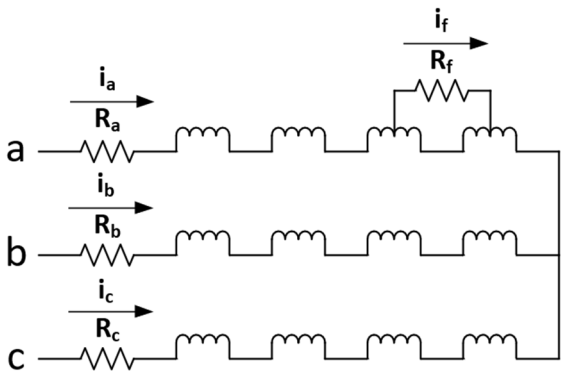

Figure 4.1 Equivalent Circuit of PMSM with inter turn short at phase-a.

By defining the vector and current vector in *abc*-reference frame as:

$$\boldsymbol{V_{sf,abc}} = \begin{bmatrix} V_a \\ V_b \\ V_c \\ 0 \end{bmatrix} \tag{4.27}$$

$$\boldsymbol{I_{sf,abc}} = \begin{bmatrix} i_a \\ i_b \\ i_c \\ i_f \end{bmatrix} \tag{4.28}$$

The corresponding resistance and inductance matrices can be derived from the equivalent circuit (Figure 4.1). The resistance matrix follows directly from Ohm's law applied to each branch of the equivalent circuit. Note that the zero in the fourth component of the voltage vector does not imply a vanishing zero-sequence voltage; its correct interpretation is based on the resistance matrix and expanded into equation (4.29), where $\left[\boldsymbol{L_f}\right] = [L \quad M \quad M]^{\mathrm{T}}$.

$$0 = i_f R_f \; - \mu R_s \left(i_a - i_f\right) - \mu \left[\boldsymbol{L_f}\right]^{\mathrm{T}} \frac{d\left[\boldsymbol{I_{sf,abc}}\right]}{dt} + \mu^2 \, L \, \frac{di_f}{dt} - \mu \frac{d}{dt} \left(\lambda_{\mathrm{PM}} \cos \theta\right) \tag{4.29}$$

The inductance matrix is derived by accounting for the self- and mutual-inductances among the three phase windings and the shorted turn set. Recall that a coil's self-inductance is proportional to the square of its turn count, whereas the mutual inductance between two coils is proportional to the product of their respective turns. Using these relations, the entries in the fourth row and column, corresponding to the short turn ratio μ, are obtained directly from the winding relations. The negative signs in the fourth column arise solely from the chosen sign convention for the fault-loop current. The resulting resistance and inductance matrix are therefore:

$$[\boldsymbol{R_{sf}}] = \begin{bmatrix} R_s & 0 & 0 & -\mu R_s \\ 0 & R_s & 0 & 0 \\ 0 & 0 & R_s & 0 \\ \mu R_s & 0 & 0 & -\mu R_s - R_f \end{bmatrix} \tag{4.30}$$

$$[\boldsymbol{L_{sf}}] = \begin{bmatrix} L & M & M & -\mu L \\ M & L & M & -\mu M \\ M & M & L & -\mu M \\ \mu L & \mu M & \mu M & -\mu^2 L \end{bmatrix} \tag{4.31}$$

The flux linkage contribution from rotor permanent magnet considering the inter-turn short fault in phase a winding given by:

$$[\boldsymbol{\lambda_{PMf,abc}}] = \lambda_{PM} \begin{bmatrix} \cos\theta \\ \cos(\theta - 2\pi/3) \\ \cos(\theta + 2\pi/3) \\ \mu\cos\theta \end{bmatrix} \tag{4.32}$$

The extended park transformation for a 4X4 matrix transformation with its inverse matrix is shown below:

(4.33)

$$[\boldsymbol{T}_{dq0f}] = \frac{2}{3}\begin{bmatrix} \cos\theta & \cos(\theta - 2\pi/3) & \cos(\theta + 2\pi/3) & \cos\theta \\ -\sin\theta & -\sin(\theta - 2\pi/3) & -\sin\theta(\theta + 2\pi/3) & -\sin\theta \\ 1/2 & 1/2 & 1/2 & 1/2 \\ 0 & 0 & 0 & 3/2 \end{bmatrix}$$

$$[\boldsymbol{T}_{abcf}] = \begin{bmatrix} \cos\theta & -\sin\theta & 1 & -2/3 \\ \cos(\theta - 2\pi/3) & -\sin(\theta - 2\pi/3) & 1 & 1/3 \\ \cos(\theta + 2\pi/3) & -\sin\theta(\theta + 2\pi/3) & 1 & 1/3 \\ 0 & 0 & 0 & 1 \end{bmatrix} \tag{4.34}$$

Following the same procedure outlined in Chapter 4.1.1, Applying the transformation $[\boldsymbol{T}] = [\boldsymbol{T}_{dq0f}] = [\boldsymbol{T}_{abcf}]^{-1}$ to both side of the equation (4.8), and substituting the *abc*-phase current vector with *dq* counterpart then yields:

$$\begin{aligned}[\boldsymbol{V}_{sf,dq0f}] = {} & \boldsymbol{T}[\boldsymbol{R}_{sf}]\boldsymbol{T}^{-1}[\boldsymbol{I}_{sf,dq0f}] + \boldsymbol{T}[\boldsymbol{L}_{sf}]\frac{d\boldsymbol{T}^{-1}}{dt}[\boldsymbol{I}_{sf,dq0f}] \\ & + \boldsymbol{T}[\boldsymbol{L}_{sf}]\boldsymbol{T}^{-1}\frac{d[\boldsymbol{I}_{sf,dq0f}]}{dt} + \boldsymbol{T}\frac{d\boldsymbol{T}^{-1}}{dt}[\boldsymbol{\lambda}_{PMf,dq0}] + \boldsymbol{T}\boldsymbol{T}^{-1}\frac{d[\boldsymbol{\lambda}_{PMf,dq0}]}{dt}\end{aligned} \tag{4.35}$$

The *dq*-axis current vector, $[\boldsymbol{I}_{sf,abc}]$, is represented by applying the Park transformation to the phase-current vector $[\boldsymbol{I}_{sf,dq0f}]$ as shown in (4.37), where the forth element i_f is the same winding path short path current in $[\boldsymbol{I}_{sf,abc}]$.

The corresponding *dq*-axis voltage vector, $[\boldsymbol{V}_{sf,dq0f}]$, is defined by considering the arrangement of resistance and inductance matrices given in (4.30) and (4.31), as shown in (4.36), where V_0 denotes the zero-sequence voltage introduced by the broken phase symmetry and $V_f = R_f i_f$ represents the voltage drop across the shorted-turn path.

$$\boldsymbol{V_{sf,dq0f}} = \begin{bmatrix} V_d \\ V_q \\ V_0 \\ V_f \end{bmatrix} \tag{4.36}$$

$$\boldsymbol{I_{sf,dq0f}} = \begin{bmatrix} i_{d,f} \\ i_{q,f} \\ 0 \\ i_f \end{bmatrix} \tag{4.37}$$

Before proceeding with the detailed derivation, below relations are introduced to provide few simplifications to the cumbersome derivation:

$$\boldsymbol{T} \cdot \frac{d\boldsymbol{T}^{-1}}{dt} \cdot \left[\boldsymbol{\lambda_{PMf,dq0}}\right] = \omega\lambda_{PM} \cdot \begin{bmatrix} 0 \\ 1 \\ 0 \\ 0 \end{bmatrix} \tag{4.38}$$

$$\boldsymbol{T} \cdot \boldsymbol{T}^{-1} \cdot \frac{d\left[\boldsymbol{\lambda_{PMf,dq0}}\right]}{dt} = \lambda_{PM} \cdot \begin{bmatrix} 0 \\ 1 \\ 0 \\ -\mu \cdot \omega_e \cdot sin(\theta) \end{bmatrix} \tag{4.39}$$

With the assistance of Wolfram Mathematica, the full *dq*-axis stator-voltage equation for a SPMSM subjected to phase-*a* inter-turn fault has been symbolically expanded and arranged as follows:

$$v_{d,f_h} = (3+\mu+\mu\cos(2\theta))(1/3)R_s i_{d,f} \quad (4.40)$$
$$-(3+\mu+\mu\cos(2\theta))(1/3)(L-M)\omega_e i_{q,f}$$
$$+(3+\mu+\mu\cos(2\theta))(1/3)(L-M)\frac{di_{d,f}}{dt}$$

$$v_{q,f_h} = \lambda_{PM}\omega_e \quad (4.41)$$
$$+(3+\mu-\mu\cos(2\theta))(1/3)R_s i_{q,f}$$
$$+(3+\mu-\mu\cos(2\theta))(1/3)(L-M)\omega_e i_{d,f}$$
$$+(3+\mu-\mu\cos(2\theta))(1/3)(L-M)\frac{di_{q,f}}{dt}$$

$$v_{d,f_f} = -(2/9)\cos(\theta)\left(3R_f + R_s(3+8\mu)\right)i_f \quad (4.42)$$
$$-(2/3)\cos(\theta)\sin(\theta)R_s\mu i_{q,f}$$
$$-(1/3)(L-M)\omega_e\mu\sin(2\theta)i_{d,f}$$
$$-(2/9)\cos(\theta)\left(-M(3+5\mu)+L(3+5\mu+3\mu^2)\right)\frac{di_f}{dt}$$
$$-(2/3)\cos(\theta)\sin(\theta)(L-M)\mu\frac{di_{q,f}}{dt}$$

$$v_{q,f_f} = -(2/3)\cos(\theta)\sin(\theta)R_s\mu i_{d,f} \quad (4.43)$$
$$+(2/9)\sin(\theta)\left(3R_f + R_s(3+8\mu)\right)i_f$$
$$-(1/3)(L-M)\omega_e\mu\sin(2\theta)i_{q,f}$$
$$-(1/3)(L-M)\mu\sin(2\theta)\frac{di_{d,f}}{dt}$$
$$+(2/9)\sin(\theta)\left(-M(3+5\mu)+L(3+5\mu+3\mu^2)\right)\frac{di_f}{dt}$$

$$
\begin{aligned}
R_f i_f = \quad & (R_s \mu \cos(\theta) - (L - M)\mu\omega_e \sin(\theta)) i_{d,f} \\
& -(R_s \mu \sin(\theta) + (L - M)\mu\omega_e \cos(\theta)) i_{q,f} \\
& -(1/3)\big(3R_f + 5R_s\mu\big) i_f \\
& +(L - M)\mu \cos(\theta) \frac{di_{d,f}}{dt} \\
& -(L - M)\mu \sin(\theta) \frac{di_{q,f}}{dt} \\
& -(1/3)\mu\big(-2M + L(2 + 3\mu)\big) \frac{di_f}{dt} \\
& -\mu\lambda_{PM}\omega_e \sin(\theta)
\end{aligned} \tag{4.44}
$$

$$
v_{0,f} = \quad -(1/3)\mu\left(R_s i_f + (L + 2M)\frac{di_f}{dt}\right) \tag{4.45}
$$

Where v_{d,f_h} , v_{q,f_h} represents the healthy part of the *dq*-axis voltage equation, and v_{d,f_f} , v_{q,f_f} denotes the contribution from the inter-turn shorted fault. The total voltage *dq*-axis governing voltage equations are given by:

$$
v_{d,f} = v_{d,f_h} + v_{d,f_f} \tag{4.46}
$$

$$
v_{q,f} = v_{q,f_h} + v_{q,f_f} \tag{4.47}
$$

By setting $R_f = 0$ and $i_f = 0$, thereby removing the fault path, equations (4.46) and (4.47) collapse to the standard *dq*-axis stator-voltage expressions for a healthy SPMSM, as given in (4.24) and (4.25). Under these conditions both the zero-sequence voltage $v_{0,f}$ and the fault-loop voltage drop $v_f = R_f i_f$ identically vanish. thereby further validates the equations from (4.40) to (4.45).

4.1.4 Inter-turn Short Fault IPMSM Governing Voltage Equations

Considering same inter-turn short fault in phase a winding as depicted in (Figure 4.1), the derivation of the *dq*-axis stator-voltage equations for an IPMSM parallels that for the SPMSM presented in the previous chapter. The major distinction is from the rotor-position-dependent inductance matrix, $L_{abc,sf}(\theta)$, defined in (4.19). When fully expanded following the same principle from last chapter, this matrix takes the following 4×4 form:

$$\left[\boldsymbol{L_{if}(\theta)}\right] = \begin{bmatrix} L_{aa}(\theta) & L_{ab}(\theta) & L_{ac}(\theta) & -\mu L_{aa}(\theta) \\ L_{ab}(\theta) & L_{bb}(\theta) & L_{bc}(\theta) & -\mu L_{ab}(\theta) \\ L_{ac}(\theta) & L_{ac}(\theta) & L_{cc}(\theta) & -\mu L_{ac}(\theta) \\ \mu L_{aa}(\theta) & \mu L_{ab}(\theta) & \mu L_{ac}(\theta) & -\mu^2 L_{aa}(\theta) \end{bmatrix} \tag{4.48}$$

For general applications, to simplify the derivation, the transformation from the three-phase voltage equations to the *dq*-axis representation for an IPMSM can be performed using the cosine-form of the inductance matrix, derived from its general form considering only the fundamental harmonic (4.20) – (4.22). However, in this work, these unique inductance matrix entities, as presented in (4.48), is employed to enable future integration into the model as an input parameter. Due to the complexity of this formulation, the calculation is carried out with the assistance of symbolic computation software.

Because rotor saliency in an IPMSM affects only the inductance variation and not the rotor flux linkage, the rotor-angle-dependent flux linkage remains the same as in an SPMSM and is given by:

$$\left[\boldsymbol{\lambda_{PMf,abc}}\right] = \lambda_{\mathrm{PM}} \begin{bmatrix} \cos\theta \\ \cos(\theta - 2\pi/3) \\ \cos(\theta + 2\pi/3) \\ \mu\cos\theta \end{bmatrix} \tag{4.49}$$

Reiterating the general stator-voltage equation from chapter 4.1.2, and applying the Park transformation as shown in (4.51). Because the inductance matrix now depends explicitly on rotor position, the resulting formulation contains an additional term that does not appear in the corresponding SPMSM derivation.

$$\begin{aligned}\left[\boldsymbol{V}_{\boldsymbol{if,abc}}\right] = \left[\boldsymbol{R}_{\boldsymbol{if,abc}}\right]\left[\boldsymbol{I}_{\boldsymbol{if,abc}}\right] + \left[\boldsymbol{L}_{\boldsymbol{if,abc}}(\theta)\right]\frac{d\boldsymbol{I}_{\boldsymbol{i,abc}}}{dt} + \frac{d\left[\boldsymbol{L}_{\boldsymbol{if,abc}}(\theta)\right]}{dt}\boldsymbol{I}_{\boldsymbol{i,abc}} \\ + \frac{d\left[\boldsymbol{\lambda}_{\boldsymbol{PM,abc}}\right]}{dt}\end{aligned} \tag{4.50}$$

$$\begin{aligned}\left[\boldsymbol{V}_{\boldsymbol{if,dq0f}}\right] = \boldsymbol{T}\left[\boldsymbol{R}_{\boldsymbol{if}}\right]\boldsymbol{T}^{-1}\left[\boldsymbol{I}_{\boldsymbol{if,dq0f}}\right] + \boldsymbol{T}\left[\boldsymbol{L}_{\boldsymbol{if}}(\boldsymbol{\theta})\right]\frac{d\boldsymbol{T}^{-1}}{dt}\left[\boldsymbol{I}_{\boldsymbol{if,dq0f}}\right] \\ + \boldsymbol{T}\left[\boldsymbol{L}_{\boldsymbol{if}}(\boldsymbol{\theta})\right]\boldsymbol{T}^{-1}\frac{d\left[\boldsymbol{I}_{\boldsymbol{if,dq0f}}\right]}{dt} + \boldsymbol{T}\frac{d\left[\boldsymbol{L}_{\boldsymbol{if}}(\boldsymbol{\theta})\right]}{dt}\boldsymbol{T}^{-1}\left[\boldsymbol{I}_{\boldsymbol{if,dq0f}}\right] \\ + \boldsymbol{T}\frac{d\boldsymbol{T}^{-1}}{dt}\left[\boldsymbol{\lambda}_{\mathbf{PMf,abc}}\right] + \boldsymbol{T}\,\boldsymbol{T}^{-1}\frac{d\left[\boldsymbol{\lambda}_{\mathbf{PMf,abc}}\right]}{dt}\end{aligned} \tag{4.51}$$

The transformation yields the same structure, but substantially lengthier equation sets than faulted SPMSM, due to the independently defined inductance entity. The complete equations are collected and rearranged below:

$$
\begin{aligned}
v_{d,f} = \quad & (1/3)R_s(3+\mu+\mu\cos(2\theta))i_{d,f} \\
& -(2/9)\cos(\theta)\Big(\big(3R_f + R_s(3+8\mu)\big)\, i_f + 3R_s\mu i_{q,f}\sin(\theta)\Big) \\
& +(1/6)\big(2L_{ab} + 2L_{ac} - 2L_{bb} - 2L_{cc} - 2L_{aa}\mu + L_{ab}\mu + L_{ac}\mu \\
& \qquad - 2L_{aa}(3+\mu)\cos(2\theta) \\
& \qquad + 2\big(L_{cc} + L_{ab}(2+\mu)\big)\cos(\pi/3+2\theta) \\
& \qquad + (4L_{ac} + 2L_{bb} + 2L_{ac}\mu)\sin(\pi/6+2\theta)\big)\omega_e i_{q,f} \\
& +(1/6)\big(\sqrt{3}L_{ab}\mu - \sqrt{3}L_{ac}\mu - 2\big(L_{bb} + L_{ac}(2+\mu)\big)\cos(\pi/6+2\theta) \\
& \qquad - 2L_{aa}(3+\mu)\sin(2\theta) \\
& \qquad + (4L_{ab} + 2L_{cc} + 2L_{ab}\mu)\sin(\pi/3+2\theta)\big)\omega_e i_{d,f} \\
& +(2/3)\big(-L_{aa}/2 + L_{aa}(1+\mu)\cos(\theta)^2 \\
& \qquad + L_{aa}\cos(2\theta) + L_{bb}\sin(\pi/6-\theta)^2 + L_{cc}\sin(\pi/6+\theta)^2 \\
& \qquad - (2+\mu)\cos(\theta)\,(L_{ab}\sin(\pi/6-\theta) \\
& \qquad + L_{ac}\sin(\pi/6+\theta))\big)\frac{di_{d,f}}{dt} \\
& -(1/9)\Big(\big(-4L_{ab} - 4L_{ac} + L_{bb} + L_{cc} - 5L_{ab}\mu - 5L_{ac}\mu \\
& \qquad + 2L_{aa}(3+5\mu+3\mu^2)\big)\cos(\theta) \\
& \qquad + \sqrt{3}\big(-2L_{ac} - L_{bb} + L_{cc} - 3L_{ac}\mu \\
& \qquad + L_{ab}(2+3\mu)\big)\sin(\theta)\Big)\frac{di_f}{dt} \\
& +(1/6)\big(\sqrt{3}L_{ab}\mu - \sqrt{3}L_{ac}\mu - 2\big(L_{bb} + L_{ac}(2+\mu)\big)\cos(\pi/6+2\theta) \\
& \qquad - 2L_{aa}(3+\mu)\sin(2\theta) \\
& \qquad + (4L_{ab} + 2L_{cc} + 2L_{ab}\mu)\sin(\pi/3+2\theta)\big)\frac{di_{q,f}}{dt}
\end{aligned}
\tag{4.52}
$$

$$
\begin{aligned}
v_{q,f} = \quad & \lambda_{PM}\omega_e \\
& -(1/3)R_s(-3-\mu+\mu\cos(2\theta))i_{q,f} \\
& -(2/9)\sin(\theta)\left(-3R_s\mu\cos(\theta)\, i_{d,f} + \left(3R_f + R_s(3+8\mu)\right) i_f\right) \\
& +(1/6)\big(-2L_{ab} - 2L_{ac} + 2L_{bb} + 2L_{cc} + 2L_{aa}\mu - L_{ab}\mu - L_{ac}\mu \\
& \qquad - 2L_{aa}(3+\mu)\cos(2\theta) \\
& \qquad + 2\big(L_{cc} + L_{ab}(2+\mu)\big)\cos(\pi/3+2\theta) \\
& \qquad + (4L_{ac} + 2L_{bb} + 2L_{ac}\mu)\sin(\pi/6+2\theta)\big)\omega_e i_{d,f} \\
& +(1/6)\big(\sqrt{3}L_{ab}\mu - \sqrt{3}L_{ac}\mu + 2\big(L_{bb} + L_{ac}(2+\mu)\big)\cos(\pi/6+2\theta) \\
& \qquad + 2L_{aa}(3+\mu)\sin(2\theta) \\
& \qquad - (4L_{ab} + 2L_{cc} + 2L_{ab}\mu)\sin(\pi/3+2\theta)\big)\omega_e i_{q,f} \\
& -(1/6)\big(\sqrt{3}L_{ab}\mu - \sqrt{3}L_{ac}\mu + 2\big(L_{bb} + L_{ac}(2+\mu)\big)\cos(\pi/6+2\theta) \\
& \qquad + 2L_{aa}(3+\mu)\sin(2\theta) \\
& \qquad - (4L_{ab} + 2L_{cc} + 2L_{ab}\mu)\sin(\pi/3+2\theta)\big)\frac{di_{d,f}}{dt} \\
& +(1/9)\Big(\big(-4L_{ab} - 4L_{ac} + L_{bb} + L_{cc} - 5L_{ab}\mu - 5L_{ac}\mu \\
& \qquad + 2L_{aa}(3+5\mu+3\mu^2)\big)\sin(\theta) \\
& \qquad + \sqrt{3}\big(2L_{ac} + L_{bb} - L_{cc} + 3L_{ac}\mu \\
& \qquad - L_{ab}(2+3\mu)\big)\cos(\theta)\Big)\frac{di_f}{dt} \\
& +(1/6)\big(-2L_{ab} - 2L_{ac} + 2L_{bb} + 2L_{cc} + 2L_{aa}\mu - L_{ab}\mu - L_{ac}\mu \\
& \qquad - 2L_{aa}(3+\mu)\cos(2\theta) \\
& \qquad + 2\big(L_{cc} + L_{ab}(2+\mu)\big)\cos(\pi/3+2\theta) \\
& \qquad + (4L_{ac} + 2L_{bb} + 2L_{ac}\mu)\sin(\pi/6+2\theta)\big)\frac{di_{q,f}}{dt}
\end{aligned}
\tag{4.53}
$$

$$
\begin{aligned}
v_{0,f} = \; & -(1/3)R_s\mu i_f \\
& +(1/6)\Big((-L_{ab}-L_{ac}+L_{bb}+L_{cc})\cos(\theta) \\
& \qquad +\sqrt{3}(-L_{ab}+L_{ac}-L_{bb}+L_{cc})\sin(\theta)\Big)\omega_e i_{q,f} \\
& +(1/6)\Big((-L_{ab}-L_{ac}+L_{bb}+L_{cc})\sin(\theta) \\
& \qquad +\sqrt{3}(L_{ab}-L_{ac}+L_{bb}-L_{cc})\cos(\theta)\Big)\omega_e i_{d,f} \\
& +(1/6)\Big((L_{ab}+L_{ac}-L_{bb}-L_{cc})\cos(\theta) \\
& \qquad +\sqrt{3}(L_{ab}-L_{ac}+L_{bb}-L_{cc})\sin(\theta)\Big)\frac{di_{d,f}}{dt} \\
& -(1/9)(L_{ab}+L_{ac}-L_{bb}-L_{cc}+3L_{aa}\mu+3L_{ab}\mu+3L_{ac}\mu)\frac{di_f}{dt} \\
& +(1/6)\Big((-L_{ab}-L_{ac}+L_{bb}+L_{cc})\sin(\theta) \\
& \qquad +\sqrt{3}(L_{ab}-L_{ac}+L_{bb}-L_{cc})\cos(\theta)\Big)\frac{di_{q,f}}{dt}
\end{aligned}
\tag{4.54}
$$

$$
\begin{aligned}
R_f i_f = \; & R_s\mu\cos(\theta)\, i_{d,f} - R_s\mu\sin(\theta)\, i_{q,f} \\
& -(1/3)\big(3R_f+5R_s\mu\big)i_f - \mu\lambda_{PM}\omega_e\sin(\theta) \\
& -\mu(-L_{ab}\cos(\pi/6-\theta)+L_{ac}\cos(\pi/6+\theta)+L_{aa}\sin(\theta))\omega_e i_{d,f} \\
& +\mu(L_{ab}\sin(\pi/6-\theta)+L_{ac}\sin(\pi/6+\theta)-L_{aa}\cos(\theta))\omega_e i_{q,f} \\
& +\mu(-L_{ab}\sin(\pi/6-\theta)-L_{ac}\sin(\pi/6+\theta)+L_{aa}\cos(\theta))\frac{di_{d,f}}{dt} \\
& -(1/3)\mu\big(L_{ab}+L_{ac}-L_{aa}(2+3\mu)\big)\frac{di_f}{dt} \\
& -\mu(-L_{ab}\cos(\pi/6+\theta)+L_{ac}\cos(\pi/6+\theta)+L_{aa}\sin(\theta))\frac{di_{q,f}}{dt}
\end{aligned}
\tag{4.55}
$$

4.1.5 PMSM Torque Equation Development

For both SPMSM and IPMSM, the torque is calculated from the product of dq-axis current and voltage, as given in (4.56). The $3/2$ scaling factor comes from the transformation of three-phase variables to the *dq*-axis, and *p* is the pole-pair count of the machine.

$$T_{mech} = \frac{P}{\omega_e} = \frac{3}{2} p\left(v_d i_d + v_q i_q\right) \tag{4.56}$$

When v_d and v_q are replaced by their SPMSM and IPMSM corresponding full *dq*-axis voltage expressions, the resulting torque formula contains additional terms proportional to $\frac{di_{d,q,f}}{dt}$, because these derivatives describe transient energy storage in the stator inductances rather than electromechanical energy conversion, their time average over a steady-state electrical cycle is zero. Consequently, only the steady-state cross-product contributes to torque production. The derivative terms are therefore retained in voltage–control and dynamic-response studies, thus they can be omitted from steady-state torque calculations without loss of accuracy.

Torque of SPMSM:

$$T_{spmsm} = T_{spmsm,h} + T_{spmsm,f} \tag{4.57}$$

$$T_{spmsm,h} = (3/2) p i_{q,f} \lambda_{PM}$$

$$T_{spmsm,f} = -(1/2)(L - M) p \mu \sin(2\theta) \left({i_{d,f}}^2 + {i_{q,f}}^2\right)$$

$$T_{ipmsm} = T_{ipmsm,h} + T_{ipmsm,f}$$

Torque of IPMSM:

$$
\begin{aligned}
T_{ipmsm} = \frac{1}{4}\Big(& i_{d,f}\Big(18\omega_e i_{d,f}\Big(\sin(2\theta)\,(-2L_{aa}(\mu+3) \\
& + L_{ab}(\mu+2) + L_{ac}(\mu+2) + L_{ac} + L_{cc}) \\
& + \sqrt{3}\cos(2\theta)\,(L_{ab}(\mu+2) - L_{ac}(\mu+2) - L_{bb} \\
& + L_{cc}) + \sqrt{3}\mu(L_{ab} - L_{ac})\Big) \\
& + \omega_e i_{q,f}\Big(\cos(2\mu)\,(-2L_{aa}(\mu+3) \\
& + L_{ab}(\mu+2) + L_{ac}(\mu+2) + L_{bb} + L_{cc}) \\
& - 2(L_{aa}\mu + L_{bb} + L_{cc}) \\
& + \sqrt{3}\sin(2\theta)\,(-L_{ab}(\mu+2) + L_{ac}(\mu+2) \\
& + L_{bb} - L_{cc}) + L_{ab}(\mu+2) + L_{ac}(\mu+2)\Big)\Big) \\
& + 2R_s {i_{d,f}}^2(\mu\cos(2\theta) + \mu + 3) \\
& + i_{q,f}\Big(2R_s i_{q,f}(-\mu\cos(2\theta) + \mu + 3) \\
& + \omega_e i_{d,f}\Big(\sin(2\theta)\,\big(-2L_{aa}(\mu+3) \\
& - \big(\sqrt{3}-1\big)L_{ab}(\mu+2) + \big(\sqrt{3}+1\big)L_{ac}(\mu+2) \\
& + \sqrt{3}L_{bb} + L_{bb} - \sqrt{3}L_{cc} + L_{cc}\big) \\
& + \cos(2\theta)\,\big(-2L_{aa}(\mu+3) \\
& + \big(\sqrt{3}+1\big)L_{ab}(\mu+2) - \big(\sqrt{3}-1\big)L_{ac}(\mu+2) \\
& - \sqrt{3}L_{bb} + L_{bb} + L_{cc} + \sqrt{3}L_{cc}\big) \\
& + \mu\big(2L_{aa} + \big(\sqrt{3}-1\big)L_{ab} - \big(\sqrt{3}+1\big)L_{ac}\big)\Big) \\
& + 2\omega_e i_{d,f}(-L_{ab} - L_{ac} + L_{bb} + L_{cc})\Big) \\
& + 6\lambda_{PM}\omega_e i_{q,f}\Big)
\end{aligned}
\tag{4.58}
$$

4.2 SPMSM Modeling within Simulink-Simscape Environment

This section details the implementation of the SPMSM model within the Simulink–Simscape environment. Because the *dq*-axis stator-voltage equations of an IPMSM share the same structure as those of an SPMSM, differing only by the additional rotor-position-dependent inductance terms, the SPMSM model is sufficient to validate the proposed modelling approach. Developing a full IPMSM model is therefore identified as a recommended avenue for future research.

4.2.1 Simulink-Simscape Language Structure

In the context of complex physical systems, custom Simscape components are designed to efficiently solving large, mixed DAE and ODE systems [33], [34]. The process begins with equation construction, where each ".ssc" file describes variables, parameters, and implicit ("acausal") equations in near-textbook form [35], [36]. When a model is compiled, Simscape intelligently concatenates these equations, applying Kirchhoff's style conservation principles to form a "square system", a state where the number of independent equations precisely matches the number of unknown variables. This process also eliminates any redundant equations, streamlining the mathematical representation. This then leads to Simscape's distinctive automatic index-1 DAE reduction, a process the software automatically simplifies a system of DAEs to a specific form that is numerically easier to solve.

A key aspect of Simscape's uniqueness is its ability to automatically tag dynamic variables and identify algebraic loops, ensuring that no Unit Delay blocks are required to break these loops. For robust simulation, especially in cases with algebraic constraints, Simscape's default global solver, "daessc", employs a consistent-state search and an implicit DAE solver capable of iteratively resolving algebraic constraints. This thereby avoids numerical residuals and solver divergence associated with artificial latency. This approach renders the state vector explicit without discrete delays. Furthermore, Simscape supports event handling and re-initialization, allowing the solver to pause, enforce algebraic consistency, and resume integration during mode changes (e.g., relays, hard stops, PWM commutations). The ability to handle algebraic loops implicitly and manage events robustly makes Simscape particularly well-suited for stiff, constraint-dominated physical networks.

As a concise example, (Figure 4.2) lists the Simscape code structure for a variable-inductance inductor.

- ***Inputs:*** Declares run-time signals, here the inductance *L*, that the block receives from its environment. Constant data would instead be placed in a parameters section and stored inside the component.
- ***Nodes:*** defines two conserving ports, p and n, through which the inductor connects to the electrical network; similar ports can be created for other physical domains when needed.
- ***Branch:*** associates the through variable with the flow between nodes p and n (e.g., current, torque, or heat transfer).
- ***Equations:*** enforces the device's physical laws, relating across variables, such as voltage, angular velocity, or temperature, to their corresponding through variables.

```
inputs
    L ={0.0, 'H'};
end

nodes
    p = foundation.electrical.electrical;
    n = foundation.electrical.electrical;
end

variables
    i = { 0, 'A' };
    v = {value = { 0, 'V' }, priority = priority.high};
end

branches
    i : p.i -> n.i;
end

equations
    assert(L > 0)
    v == p.v - n.v;
    v == L*i.der
end
```

Figure 4.2 Simscape code structure example.

To note that In Simscape component the double-equals sign "==" denotes an algebraic equality that must hold continuously during simulation, not an assignment as in conventional programming languages.

4.2.2 SPMSM Simscape Component Modeling

Attached in the APPENDIX A, is the Simscape code for compiling the adjustable turn fault SPMSM model.

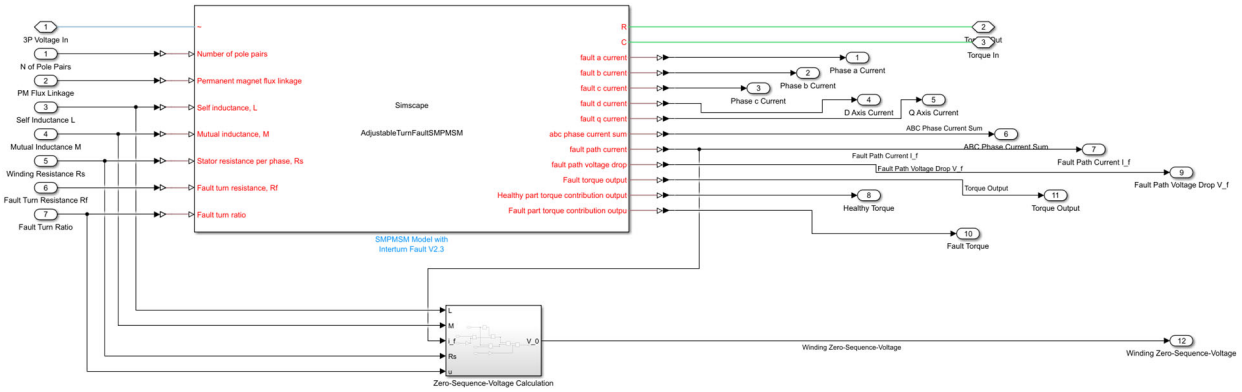

(a)

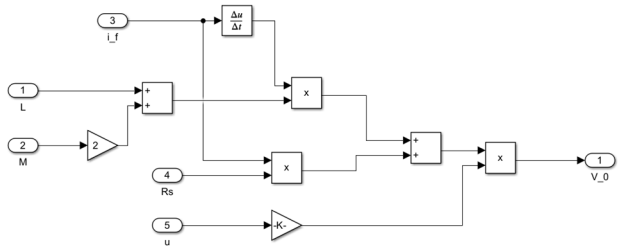

(b)

Figure 4.3 (a) Simscape component model of SPMSM (b) Zero-sequence-voltage calculation subsystem outside of the Simscape component model

Attached in Appendix A is the Simscape code for compiling the adjustable turn fault SPMSM model. Within this code, the input three-phase voltage is transformed into a dq-axis voltage vector. From this vector, its v_d , v_q with corresponding equations derived from Chapter 4.1.3 and a third implicit equation representing the short-path voltage drop as detailed in the same chapter, Equation (4.44), collectively form a previously described square system. The three unknowns to be solved are the d-axis current, q-axis current, and the fault path current. These solved currents are then utilized to apply current properties to the machine input terminals and to reinforce the Kirchhoff's Current Law (KCL) condition for the wye-connected machine.

For the last unused entity from the fourth-order dq-axis voltage vector, the zero-sequence voltage, it cannot be directly incorporated into the square system. This limitation arises because, within this particular model structure, the actual v_0 value is derived instantaneously from the controller-side input voltage. In contrast, its calculation within the model is based on currents solved from the square system, resulting in a discrepancy between the directly transformed and calculated values. Consequently, the zero-sequence voltage cannot be utilized as one of the constraints within the square system.

Another important consideration stems from Simscape's unique automatic index-1 DAE reduction feature: only a limited number of derivative terms are permissible within the model itself. These derivative terms are exclusively utilized for solving the core square system; any derivative terms appearing outside this context will trigger an error. Consequently, for any post-simulation calculations involving derivative terms that are intended for result visualization or analysis, these computations must be performed externally to the Simscape components. As illustrated in Figure 4.3 (b), the zero-sequence voltage is calculated outside the main Simscape block.

Lastly, the proposed SPMSM Simscape components are meticulously modeled to allow all machine parameters to be conveniently defined externally to the block. This design choice facilitates effortless adjustment of machine parameters during the subsequent machine learning model training stage. Furthermore, the short-path resistance, R_f, can be to any desired value, enabling the simulation of varying degrees of winding insulation failure. By setting both the short-turn ratio and R_f to zero or a negligible value, the model effectively reverts to representing a healthy SPMSM.

Chapter 5
PMSM Control Strategy and Stator Turn Fault Simulation Controller Design

In a PMSM operating under a constant torque command, the q-axis current reference, Iq, is maintained at a constant value within the synchronously rotating dq-reference frame. This condition arises from the principle of field-oriented control, wherein the stator current space vector is held at a fixed, typically orthogonal relationship, to the rotor flux linkage vector. Because this reference frame is precisely aligned with the rotor's electrical angle, a constant i_q directly corresponds to a constant electromagnetic torque, thereby demonstrating the synchronous operation of the drive.

The optimal relationship between the d-axis current and the q-axis current is highly dependent on the rotor's saliency. For SPMSMs, which exhibit negligible saliency ($L_d = L_q$) the maximum torque per ampere (MTPA) strategy corresponds to an operating point of $i_d = 0$. While this characteristic simplifies the implementation of the current control loop, it inherently limits the machine's torque density compared to interior-rotor designs that can leverage reluctance torque.

In contrast, Interior IPMSMs and SynRMs are characterized by their pronounced rotor saliency. For these machines, the total electromagnetic torque includes a significant reluctance torque component in addition to the magnetic torque. Consequently, achieving MTPA requires a more complex control strategy where both the d-axis and q-axis currents are actively manipulated. The optimal operating point is no longer fixed at $i_d = 0$ but is instead determined by a nonlinear relationship that considers machine parameters, magnetic saturation effects, and the specific torque command.

A further control complication arises when the motor must operate above its rated base speed, entering the constant power region. At such elevated speeds, the back-electromotive force (back-EMF) generated by the rotor's permanent magnets can approach or exceed the inverter's DC bus voltage limit. To maintain controllability and prevent an over-voltage fault, a flux-weakening

strategy must be employed. Flux weakening is accomplished by injecting a negative d-axis current. This current generates a magnetic field that directly opposes the permanent magnet flux linkage, effectively reducing the net air-gap flux and, consequently, the magnitude of the back-EMF. While this technique is applicable to all PMSM topologies, it is particularly effective in IPMSMs. The inherent saliency of an IPMSM means that a negative i_d not only weakens the flux but also contributes a beneficial reluctance torque component. This additional torque helps sustain the motor's output capability at high speeds, even as the magnet torque component diminishes. The implementation demands precise coordination between the d-axis and q-axis currents. An overly aggressive injection of negative i_d can degrade efficiency and impose excessive current stress on the inverter hardware. Conversely, an insufficient flux-weakening command will fail to constrain the back-EMF, preventing the machine from reaching its high-speed operating point. Therefore, the control algorithm must carefully balance these competing objectives.

In summary, constant-torque operation in PMSMs is considerably simplified for SPMSMs, owing to their zero-saliency condition and the resulting effectiveness of an $i_d = 0$ control strategy. For salient-pole machines, namely IPMSMs and SynRMs, the dynamic relationship between i_d and i_q is essential. It must first satisfy the MTPA criterion at low-to-medium speeds and subsequently enable flux-weakening operation above base speed. A rigorous understanding of these current-vector relationships is thus a fundamental prerequisite for designing high-performance PMSM drive systems.

5.1 Field-oriented Control (FOC)

Field-Oriented Control (FOC), also known as vector control, is a sophisticated motor control strategy that enables high-performance control of AC synchronous and induction motors.

Its development revolutionized the field of electric drives, allowing AC motors to achieve the precise and rapid torque response that was once only possible with DC motors.

FOC is built on the notion of the space vector. Although its algebraic form mirrors classical phasor notation, the two constructs address fundamentally different problems. The space vector $\boldsymbol{f_{abc}}$, restating the equation from Chapter 2.1.1 as equation (2.1), is a time-domain object, at every sampling instant it combines the three instantaneous phase values into a single complex number that preserves their amplitude and spatial orientation. Phasor notation, by contrast, is a frequency-domain tool, it represents a strictly sinusoidal signal of fixed frequency with a constant complex amplitude (typically in RMS) and phase.

The vector $\boldsymbol{f_{abc}}$ is expressed in the complex form, which aligns with the representation of stationary $\alpha\beta$-axis in the complex plane denoted by (5.2). This transforms the three-phase quantity time domain quantity into ab complex plane.

$$\boldsymbol{f_{abc}} \equiv \frac{2}{3}(f_a + \boldsymbol{a} f_b + \boldsymbol{a^2} f_c) \tag{5.1}$$

$$\boldsymbol{f_{abc}} = f_\alpha + j f_\beta \tag{5.2}$$

To implement control, it is mathematically rotated into a reference frame synchronized with the rotor flux $\boldsymbol{f_{dq}}$ by multiplying it by the operator $e^{-j\theta}$.

$$\boldsymbol{f_{dq}^{\omega}} = \boldsymbol{f_{abc}} \cdot e^{-j\theta} = f_d + j f_q \tag{5.3}$$

This transformation can also be done through the Clark-Park matrix transformation where the space vector $\boldsymbol{f_{abc}}$ is also in its matrix form.

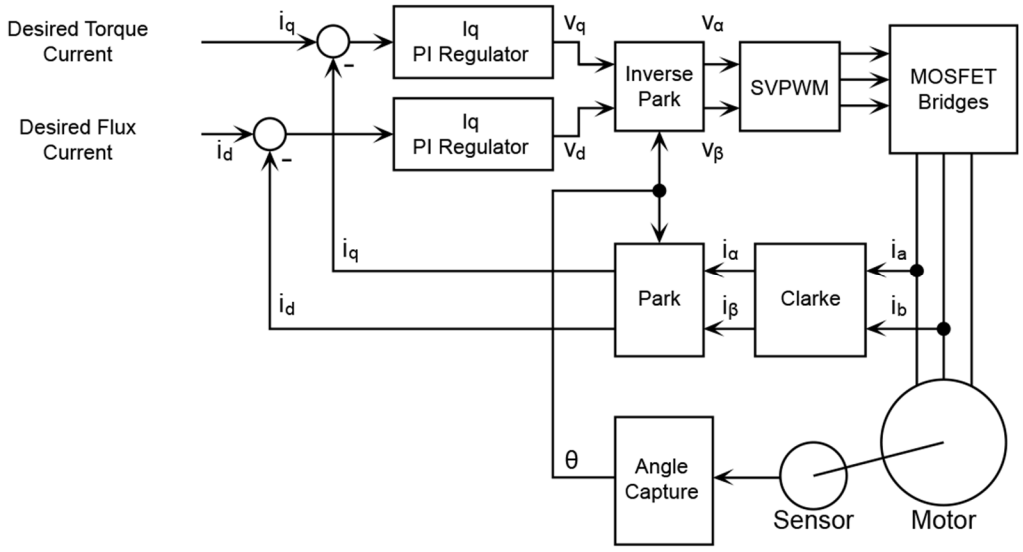

Figure 5.1 Control block diagram of Field-Oriented Control (FOC) [37]

Figure 5.1 depicts the overall logic of FOC. The phase currents i_a, i_b are precisely measured with its phase C current be calculated by KCL. The phase currents are first converted into a two-phase stationary system i_α, i_β by the Clarke transform. Then, using the measured rotor electrical angle, the Park transform rotates these stationary components into the *dq*-rotating-reference frame. yielding the feedback currents for flux i_d and torque i_q that correspond to reluctance torque and field torque. The difference of current command reference and its feedback being compared and inject into the PI controllers to generate control voltage v_d, v_q which is being inversely transformed by inverse park transformation. The PWM modulator takes the stational v_α, v_β to generate the gate control signal for VCCSI drive the machine. This concludes the whole FOC control cycle.

The block diagram in Figure 5.1 depicts the overall logic of FOC. The process begins with the measurement of the phase-*a* and -*b* currents i_a, i_b, from which the phase-*c* current is calculated using Kirchhoff's Current Law (KCL). These three phase currents are then transformed into a two-phase stationary reference frame i_α, i_β by the Clarke transform. Subsequently, using the measured

rotor electrical angle (θ), the Park transform rotates these stationary components into the dq-rotating-reference frame. This yields the feedback currents for flux-producing, (i_d) and torque-producing (i_q). For a salient motor like an IPMSM, the total electromagnetic torque is a function of both currents, comprising both magnet (or field) torque and reluctance torque.

These feedback currents are compared to their respective command references (i_d* ,i_q*). The resulting error signals are fed into two independent PI controllers, which generate the required control voltages, v_d and v_q . These voltages are then transformed back into the stationary α−β frame by the Inverse Park transform. Finally, a PWM module uses the v_α and v_β commands as reference to generate gate control signals depending on different modulation method for the current-controlled voltage source inverter (CCVSI) to drive the machine. This constitutes the entire FOC control cycle.

5.2 Operation Region of PMSM in Current Plane at d-q Reference Frame

The AC phase voltage output of a three-phase PWM inverter is inherently limited by its input DC bus voltage (V_{dc}) due to the inverter's physical design, or topology. When Discontinuous PWM (DPWM) or Space Vector PWM (SVPWM) is used, the maximum achievable phase voltage (V_{smax}) is defined by the equation:

$$V_{smax} = \frac{V_d}{\sqrt{3}}\eta \tag{5.4}$$

In (5.4), η represents the voltage-utilization factor. To ensure stable performance, this factor is typically kept within a safe operating margin of 0.90 to 0.95. This allows the inverter to reliably synthesize a high-quality AC voltage, balancing maximum output with operational safety.

When the maximum phase voltage V_{smax} is constrained by the inverter's DC-bus voltage V_{dc} , the stator *dq*- or *αβ*– voltage components must satisfy (5.5); regardless of reference frame:

$$V_{ds}^{s*2} + V_{qs}^{s*2} = V_{ds}^{r*2} + V_{qs}^{r*2} = V_{ds}^{e*2} + V_{qs}^{e*2} \leq V_{smax}^{2} \tag{5.5}$$

Following the same principle, the stator current components in the *dq*- or *αβ*- reference frame is constrained by (EQ), The corresponding peak phase current I_{smax} is dictated by the maximum current rating of the inverter's power-semiconductor devices.

$$i_{ds}^{s*2} + i_{qs}^{s*2} = i_{ds}^{r*2} + i_{qs}^{r*2} = i_{ds}^{e*2} + i_{qs}^{e*2} \leq I_{smax}^{2} \tag{5.6}$$

Two operating boundaries, one for voltage and one for current, are defined by (5.5) and (5.5) and can both be represented in the *dq*-reference frame. It is difficult to track both constrains on two separate planes simultaneously. Due to the nature that torque is usually correspond to current which cannot be naturally visualized in the voltage plane [38]. Moreover, the current-plane boundary is expressed in terms of V_{smax}, which can be determined unambiguously from the DC-bus voltage. For these reasons, limits of the *dq*-axis components are usually analyzed in the *dq*-axis current plane rather than in the voltage plane.

Restating the *dq*-axis winding voltage equations for IPMSM from pervious chapters:

$$v_d = r_s i_d + L_d \frac{di_d}{dt} - \omega_e L_q i_q \tag{5.7}$$

$$v_q = r_s i_q + L_q \frac{di_q}{dt} + \omega_e L_d i_d + \omega_e \lambda_{PM} \tag{5.8}$$

Assuming the IPMSM is operating under steady-state condition or a very current variation, the time derivative terms, di/dt, can be neglected. This simplifies the equations to:

$$\left(R_s i_{ds} - \omega_e L_q i_{qs}\right)^2 + \left(R_s i_{ds} + \omega_e L_q i_{qs} + \omega_e \lambda_{PM}\right)^2 \leq V_{smax}^2 \tag{5.9}$$

After fully expanding the equation (5.9) and rearranging the terms, the voltage constraint can be expressed in terms of the current:

$$Z_{ds}^2\left(i_{ds} + \frac{\omega_e^2 L_d \lambda_{PM}}{Z_{ds}^2}\right)^2 + Z_{qs}^2\left(i_{qs} + \frac{\omega_e R_s \lambda_{PM}}{Z_{qs}^2}\right)^2 + 2\omega_e R_s\left(L_d - L_q\right) i_{ds} i_{qs} \leq V_{smax}^2 \tag{5.10}$$

Where $Z_{ds}$and Z_{qs} are defined as:

$$Z_{ds} \equiv \sqrt{R_s^2 + (\omega_e L_d)^2} \tag{5.11}$$

$$Z_{qs} \equiv \sqrt{R_s^2 + \left(\omega_e L_q\right)^2} \tag{5.12}$$

Equation (5.10) can be rewritten into the form of (5.13), which represents the voltage-limit ellipse shown in (Figure 5.2). The ellipse's center is located at (5.14), and its major axis is rotated from the *d*-axis by an angle of (5.15). On the same *d-q* axis current plane, the current-limit circle of the IPMSM can also be plotted. This constraint forms a circle centered at the origin with a radius of i_{smax}.

$$\begin{aligned} Z_{ds}^2\left(i_{ds} + \frac{\omega_e^2 L_q \lambda_{PM}}{R_s^2 + \omega_e^2 L_d L_q}\right)^2 + Z_{qs}^2\left(i_{qs} + \frac{\omega_e R_s \lambda_{PM}}{R_s^2 + \omega_e^2 L_d L_q}\right)^2 \\ + 2\omega_e R_s\left(L_d - L_q\right)\left(i_{ds} + \frac{\omega_e^2 L_q \lambda_{PM}}{R_s^2 + \omega_e^2 L_d L_q}\right)\left(i_{qs} + \frac{\omega_e R_s \lambda_{PM}}{R_s^2 + \omega_e^2 L_d L_q}\right) \\ \leq V_{smax}^2 \end{aligned} \tag{5.13}$$

$$\left(-\frac{\omega_e^2 L_q \lambda_{PM}}{R_s^2 + \omega_e^2 L_d L_q}, -\frac{\omega_e R_s \lambda_{PM}}{R_s^2 + \omega_e^2 L_d L_q}\right) \tag{5.14}$$

$$\frac{1}{2}\tan^{-1}\frac{2R_s}{\omega_e(L_d+L_q)} \tag{5.15}$$

The derivation shown above, referenced from [5], presents a comprehensive method for defining the voltage-limit ellipse. A more common simplification is often employed, particularly for high-speed operation in the field-weakening region. In this regime, the system operates above its base speed, causing the reactive voltage drops to become dominant. Consequently, the stator resistance terms can be considered negligible. This assumption greatly simplifies the derivation, the result is shown as below:

$$(\omega_e L_d)^2\left(i_{ds}+\frac{\lambda_{PM}}{L_d}\right)^2+\left(\omega_e L_q\right)^2 i_{qs}^2 \le V_{smax}^2 \tag{5.16}$$

$$\left(i_{ds}+\frac{\lambda_{PM}}{L_s}\right)^2+i_{qs}^2 \le \frac{V_{smax}^2}{\omega_e^2 L_s^2} \tag{5.17}$$

In the case of SMPMSM, because its d and q axis inductance are identical, that is $L_d = L_q = L_s$. (5.13) can be further simplified into (5.16). The Voltage-limit ellipse is center is at (5.17), and both Voltage-limit ellipse and Current-limit is plotted at (Figure 5.2)

$$\left(i_{ds}+\frac{\omega_e^2 L_s \lambda_{PM}}{R_s^2+\omega_e^2 L_s^2}\right)^2+\left(i_{qs}+\frac{\omega_e R_s \lambda_{PM}}{R_s^2+\omega_e^2 L_s^2}\right)^2 \le \frac{V_{smax}^2}{R_s^2+\omega_e^2 L_s^2} \tag{5.18}$$

$$\left(-\frac{\omega_e^2 L_s \lambda_{PM}}{R_s^2+\omega_e^2 L_s^2}, -\frac{\omega_e R_s \lambda_{PM}}{R_s^2+\omega_e^2 L_s^2}\right) \tag{5.19}$$

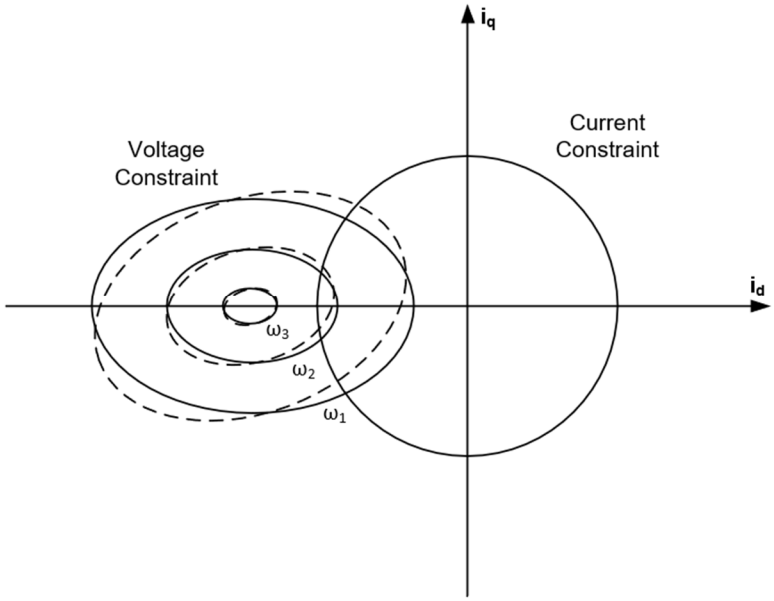

(a)

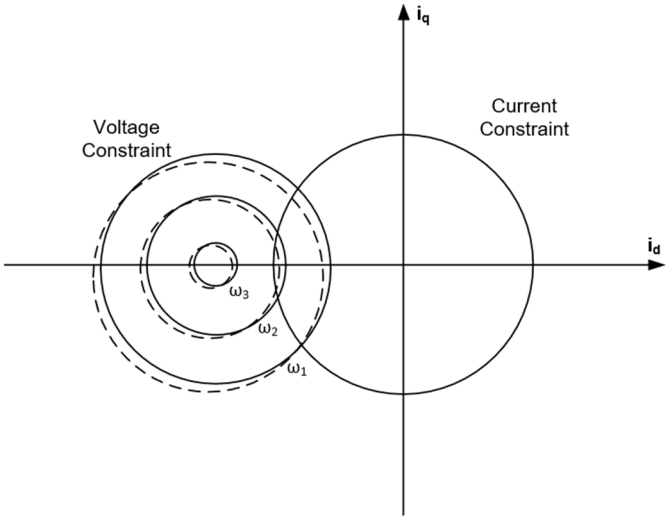

(b)

Figure 5.3 Voltage and current constraints of PMSM depicted in a current plane. (a) Interior permanent magnet synchronous machine (IPMSM). (b) Surface-mounted permanent magnet synchronous machine (SPMSM).

5.2.1 Maximum Torque per Ampere (MTPA) MTPV Control, Flux weakening

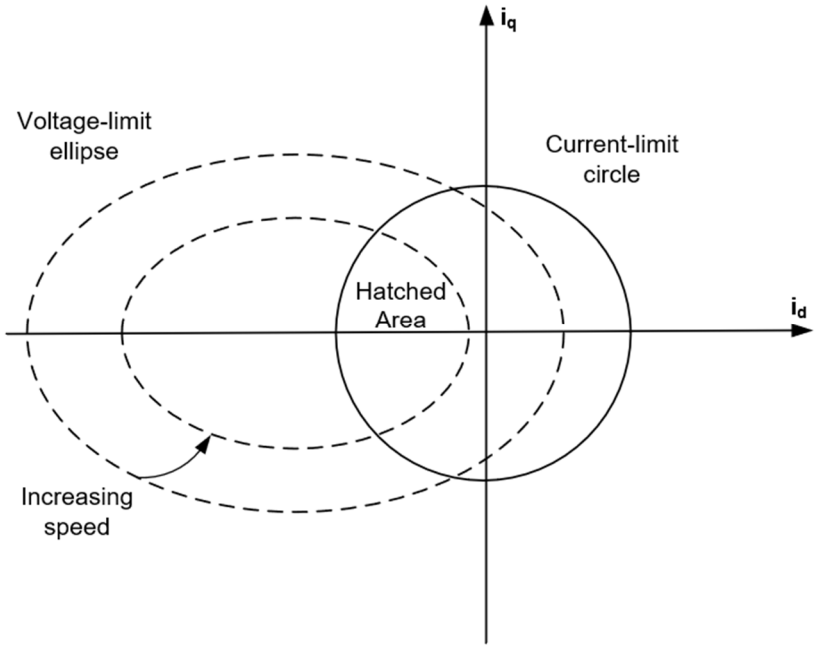

Figure 5.3 Voltage and current constraints of PMSM machine depicted in a current plane demonstrating speed effect

As established in pervious chapter, the operational limits of a PMSM are defined by its voltage and current constraints. These constraints are decided by machine's intrinsic parameters and the its inverter's hardware capacity. Both of these limits can be graphically represented on the d-q axis current plane where any PMSM operating point is defined by a current space-vector with its corresponding d-axis and q-axis components. Following equations (5.14) and (5.19), the boundary of the voltage-limit ellipse shrinks with higher electrical speed ω for both IPMSM and SPMSM, while the current-limit circle is at the center of the coordinate with a constant radius I_{smax} from (5.7). The feasible operating region of a PMSM is the commonly hatched area, formed by the intersection of the voltage-limit ellipse and the current-limit circle. Any operating current vector for the PMSM must remain within this area, in order to satisfy both voltage and current constrain.

Base on the simplified voltage-limit ellipse derivation (5.18) and (5.19), the resistive term is neglected, which indicates the center of the voltage-limit ellipse is fixed regardless its electrical speed $\omega_e$which only contributes to its boundary change. As shown in Figure 5.4 (2), in a finite-speed drive system, the center of the voltage-limit ellipse lies outside the current-limit circle. As the electrical speed ω_e increases, the ellipse shrinks until its boundary no longer overlaps with the current-limit circle. At that point, there is no longer a feasible operating region, which means this type of drive has a maximum operating speed defined by its electrical constraints. On the other hand, in an infinite-speed drive system, depicted in Figure 5.4 (b), the center of the voltage-limit ellipse is contained within the current-limit circle. This means that no matter how much the ellipse shrinks with increasing speed, a feasible operating region always exists. Therefore, the machine can ideally operate up to an infinite speed without being limited by its voltage or current constraints.

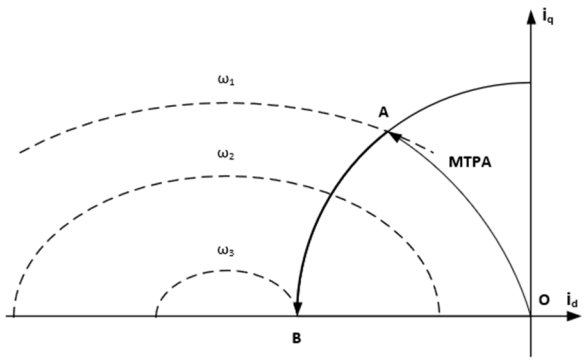

(a)

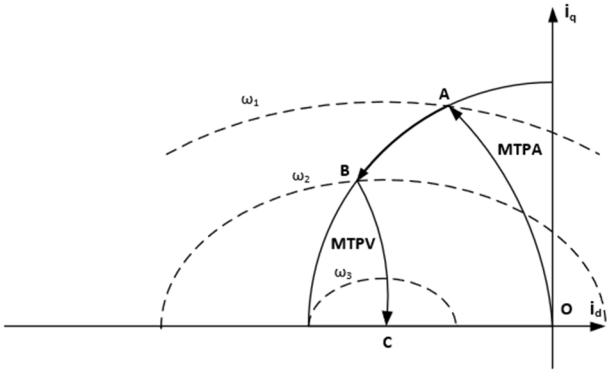

(b)

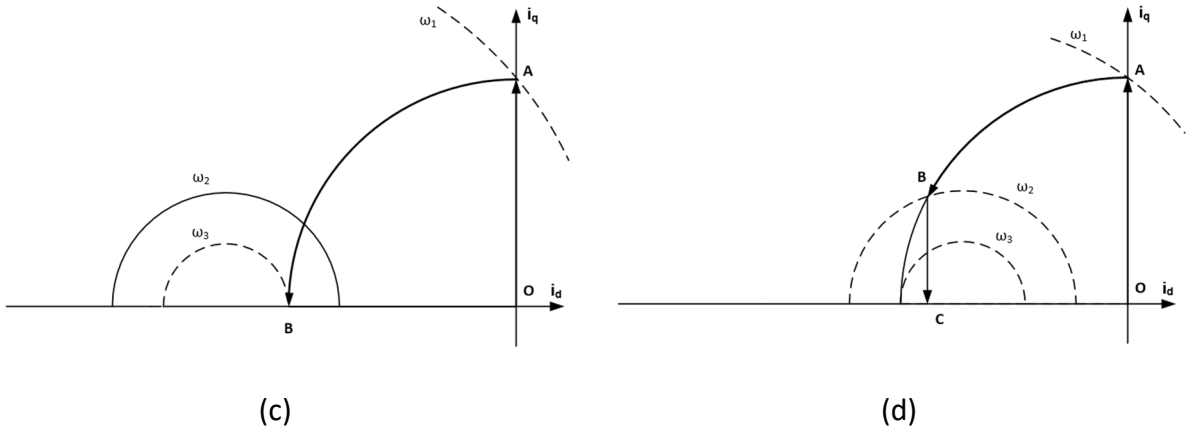

Figure 5.4 Operating regions according to the parameters of the permanent magnet AC machines. (a) IPMSM (finite-speed drive system). (b) IPMSM (infinite-speed drive system). (c) SMPMSM (finite-speed drive system). (d) SMPMSM (infinite-speed drive system).

For IPMSM, as illustrated in Figure 5.4 (a), when a finite-speed drive system accelerates from a standstill, the d-q axis current space vector moves along the Maximum Torque per Ampere (MTPA) trajectory, OA. This continues until the speed increases to a point where the boundary of the voltage-limit ellipse intersects the current-limit circle, at point A, at its base speed. To operate at higher speeds, the controller enters the flux-weakening region due to a higher back-EMF generated by parament magnet. The current space vector then moves from A towards B along the current-limit circle. As the speed continues to increase, the voltage ellipse shrinks further, with the operating point eventually reaching point B, which represents the maximum achievable speed for the system. In the case of an infinite-speed drive Figure 5.4 (b), a Maximum Torque per Voltage (MTPV) trajectory is introduced where the system is purely voltage-limited unit it reaches its ideal infinite-speed.

For SPMSM, the MTPA, Flux weakening and MTPV operation follows the same sequence. The key difference is the optimal MTPA strategy for a non-salient SPMSM is to set the d-axis current to zero, as only the q-axis current produces torque. A consequence of this is that the base

speed point A lies on the q-axis, where the voltage-limit ellipse and current-limit circle meet in Figure 5.4 (c). It can also be observed from Figure 5.4 (d), the straight, vertical optimal MTPV trajectory implies the absence of reluctance torque control due to SPMSM's non-salient structure.

It is important to note that the optimal MTPA and MTPV trajectories for an IPMSM are determined either analytically or experimentally. One of the foundational researches on PMSM operating limits, "Expansion of Operating Limits for Permanent Magnet Motor by Current Vector Control Considering Inverter Capacity", established the analytical method for these trajectories, which has since been the basis for extensive subsequent research.

5.3 Pulse-width-modulation (PWM) Strategies

The standard technique for generating Pulse Width Modulation (PWM) signals involves utilizing the on/off action of semiconductors to compare a reference signal with a carrier signal. As depicted in Figure 5.5, this method, known as carrier-based Sinusoidal PWM (SPWM), compares a low-frequency sinusoidal reference signal with a high-frequency triangular wave carrier signal.

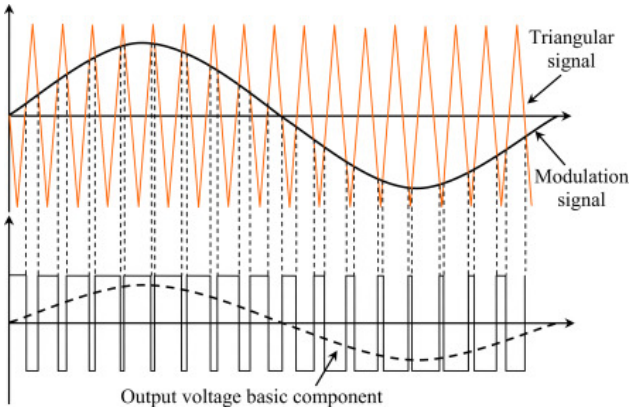

Figure 5.5 Illustration of SPWM generation by comparison of modulation signal [40]

The relationship between these two signals is defined by the modulation index m, which is the ratio of the reference signal's amplitude to the carrier signal's amplitude

$$m = \frac{V_{\text{ref}}}{V_{\text{carrier}}} \tag{5.20}$$

As established by [41], the peak amplitude of the fundamental component of the inverter's output phase voltage $V_{\text{out, peak}}$ is directly proportional to this modulation index and the DC bus voltage V_{dc}:

$$V_{\text{out, peak}} = m \cdot \frac{V_{dc}}{2} \tag{5.21}$$

The inverter driving a PMSM employs more advanced PWM strategies to transform the DC bus voltage into a three-phase AC voltage. These methods utilize the inverter's three switch pairs to generate the required output voltage for controlling PMSM's current space vector. The two most commonly implemented of these PWM techniques are detailed in the subsequent chapter.

5.3.1 Space Vector PWM (SVPWM)

Figure 5.6 illustrates a common three-phase Voltage Source Inverter (VSI) topology. This inverter consists of three legs, with each leg comprising an upper and a lower switch. For each leg, the switching state can be defined as "1" when the upper switch is on (connecting the output to the positive DC rail) or "0" when the lower switch is on (connecting to the negative DC rail). To prevent a short circuit or "shoot-through" condition in a leg, a dead-time must be implemented during the transition between states. Taking the reference vector v_α, v_β from the Inverse Park transformation, as demonstrated in Figure 5.7, the three-phase voltage output must be synthesized

to match this reference space vector. To achieve this, the SVPWM hexagon is used to illustrate the relationship between the VSI's switching states and the produced space vector.

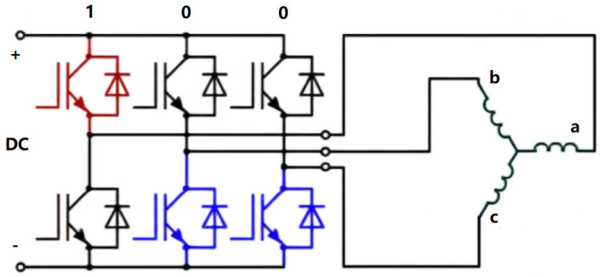

Figure 5.6 Illustration of a common voltage source inverter (VSI) topology

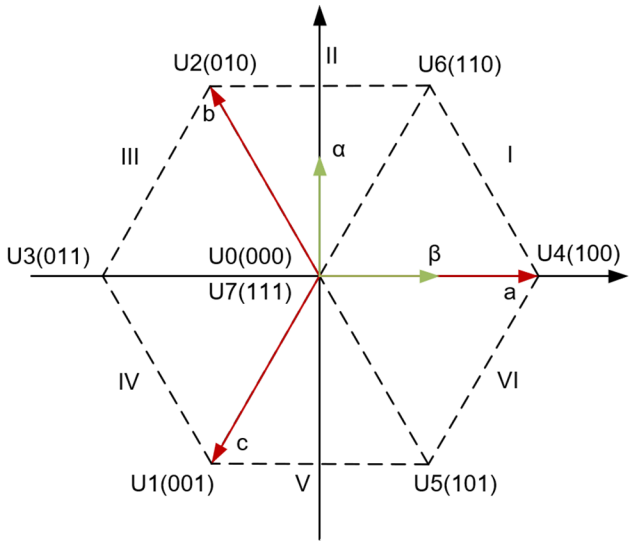

Figure 5.7 Voltage space vectors and switching states of a two-level VSI

$$v_{an} = +\frac{V_{dc}}{2}$$

$$v_{bn} = +\frac{V_{dc}}{2} \tag{5.22}$$

$$v_{cn} = -\frac{V_{dc}}{2}$$

$$v_{\alpha\beta} = \frac{2}{3}(v_{an} + a \cdot v_{bn} + a^2 \cdot v_{cn}) \tag{5.23}$$

$$v_a + jv_b = \frac{V_{dc}}{3} + \frac{\sqrt{3}}{3}V_{dc} = \frac{2}{3}V_{dc}e^{j60^\circ} \tag{5.24}$$

This concept is best explained with an example. Consider the inverter switching state (110), where the phase terminal line- neutral voltage output is (5.24) which is equivalent to (5.25) derived at a-b plane. All seven-switching states of VSI and its equivalent ab plane space vector is shown in table (Table 5.1)

Table 5.1 VSI space vector switching states

State (S_a S_b S_c)	**Complex form $V_x = v_a + jv_b$**	**Angle**
100	$\frac{2}{3}V_{dc}$	0°
110	$\frac{2}{3}V_{dc}e^{j60^\circ}$	60°
010	$\frac{2}{3}V_{dc}e^{j120^\circ}$	120°
011	$\frac{2}{3}V_{dc}e^{j180^\circ}$	180°
001	$\frac{2}{3}V_{dc}e^{j240^\circ}$	240°
101	$\frac{2}{3}V_{dc}e^{j300^\circ}$	300°
000,111	0	-

To synthesize an arbitrary reference space vector $\vec{U}_{ref}$ at any phase angle, SVPWM approximates it as a time-averaged sum of three adjacent inverter switching states from the SVPWM hexagon. As illustrated in Figure 5.8, $\vec{U}_{ref}$ is generated by controlling the duty cycles of the two active vectors that bound the sector it lies in, along with the zero vectors.

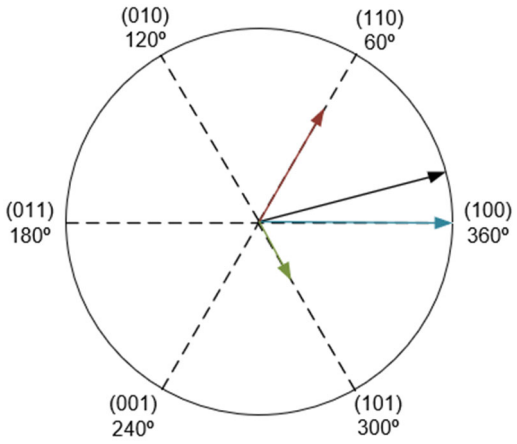

Figure 5.8 Illustration of space vector decomposition in switching states

The foundational paper SVPWM: [42] illustrates the detailed mathematical calculation required to synthesize any reference vector, $\vec{U}_{ref}$. The process involves determining two key parameters: the angle of the reference vector within its switching sector (γ) and the modulation index (a), which is given by:

$$a = \frac{|\vec{U}_{ref}|}{\sqrt{\frac{2}{3}}U_d} \tag{5.25}$$

From these parameters, the time durations for the first active vector T_1, the second active vector T_2, and the zero vector T_0 are calculated as follows:

$$T_2 = T_Z \cdot a \cdot \frac{\sin \gamma}{\sin 60^\circ} \tag{5.26}$$

$$T_1 = T_Z \cdot a \cdot \frac{\sin(60^\circ - \gamma)}{\sin 60^\circ}$$

$$T_0 = T_Z - T_2 - T_1$$

Here, T_Z is the inverter's base switching period. The final switching sequence is then selected based on two rules designed to minimize switching losses: only one switch should change state at a time, and the pattern should be symmetrical.

5.3.2 Discontinuous PWM (DPWM)

Discontinuous Pulse Width Modulation (DPWM) is a family of modulation techniques that are variations of SVPWM primarily designed to improve the efficiency of a power inverter by reducing its switching losses [43]. The core principle of DPWM is to "clamp" one of the three inverter phases for a portion of the fundamental electrical cycle, typically for 120 out of 360 degrees. During this clamped period, the switches for that phase are held continuously ON and do not operate, which means no switching losses occur in that leg of the inverter.

The main difference from SVPWM lies in this behavior. As demonstrated by [44], both continuous methods like SVPWM and discontinuous methods like DPWM can be understood within a unified framework. Whereas SVPWM continuously switches all three phases to produce the smoothest possible output waveform and achieve maximum voltage utilization, DPWM intentionally stops switching one phase to prioritize inverter efficiency. This creates a trade-off: SVPWM generally offers lower current distortion and the best motor performance, while DPWM offers higher inverter efficiency and reduced thermal stress on the power electronics.

5.4 Issue with Open-loop-controlled PMSM Simulation

In some simulation model building practices, initial model verification is often conducted in an open-loop controlled environment. This approach is typically employed as a preliminary step to isolate the dynamic behavior of the system from controller effects, allowing for observation of the model's inherent response to inputs. However, this methodology presents significant limitations when applied to PMSM modelling. An open-loop PMSM model fundamentally relies on a pre-defined frequency for the injected three-phase voltage, implicitly assuming that the rotor will synchronize with this frequency. Yet, in the absence of actual rotor position feedback, discrepancies between the injected voltage frequency and the rotor's actual speed or initial position, particularly under load conditions, can lead to numerous operational issues.

A primary issue encountered is the lack of synchronization. Within the proposed PMSM Simscape component, the actual angular velocity is derived from the output physical shaft of the rotor, and this is then directly linked to the machine's electrical angle, which is subsequently used in the Park transformation for *dq*-axis current calculations. The machine shaft is inherently coupled to the load dynamics. In an ideal, unloaded open-loop scenario, a constant injected frequency should theoretically lead to the rotor eventually synchronizing and rotating at a speed corresponding to that frequency, thereby allowing the actual electrical angle to align with the commanded electrical angle. However, in this simulation context, the rotor angle is not externally linked to the injected voltage frequency, and its initial position is inherently unknown. Given that the rotor shaft is connected to a load dynamic model, any initial misalignment will prevent the machine from achieving its synchronized operating state. This desynchronization can introduce substantial and incorrect distortions into the phase currents, as illustrated in Figure 5.9. Furthermore, considering the load applied to the model, if the load torque or initial conditions are

unfavorable, the machine may fail to operate correctly, leading to highly distorted and unbalanced currents.

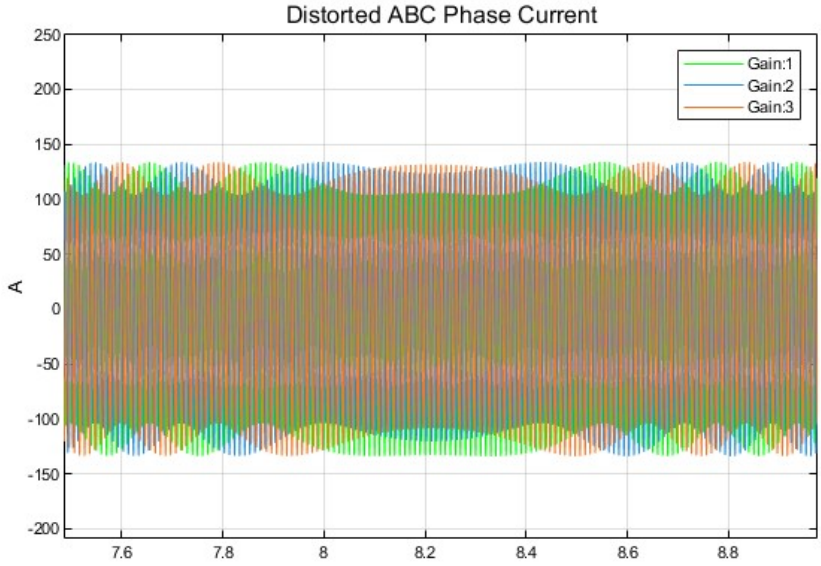

Figure 5.9 Distorted abc-phase current from improper synchronized open-loop-controlled SPMSM

Another significant concern is the propensity for oscillations and instability. Without the corrective actions of a closed-loop controller, even minor disturbances or parameter mismatch can precipitate oscillations in both speed and current, culminating in unbalanced current waveforms. The absence of a closed-loop control mechanism prevents the machine from converging to a stable operating point, ultimately leading to a divergent machine state that deviates significantly from its intended or correct operational trajectory.

Feasible as it may be to model a PMSM under open-loop control, such an approach inherently requires precise and extensive parameter calibration. Consequently, the proposed SPMSM model is designed and developed directly within a closed-loop controlled environment.

5.5 Close-loop-controlled SPMSM Simulation Model and Results

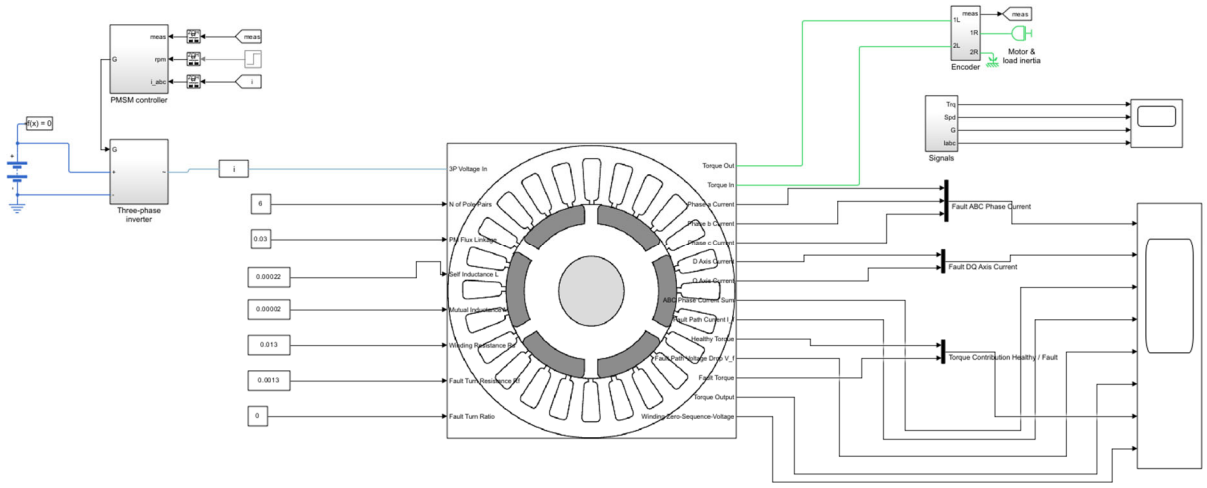

Figure 5.10 Overview of the Simulink control system with SPMSM model integrated

Figure 5.10 illustrates the closed-loop system architecture for the proposed Surface-Mounted Permanent Magnet Synchronous Machine (SPMSM), which incorporates speed-controlled Field-Oriented Control (FOC) with Space Vector Pulse Width Modulation (SVPWM). The associated system parameters are comprehensively summarized in Table 5.2.

Table 5.2 Parameters of proposed simulation model

Class	Item	Value
SPMSM	Pole Number	6
	Maximum Power (W)	2827
	Maximum Torque (Nm)	40
	Stator Winding Resistance Rs (mΩ)	13
	Stator Mutual-Inductance (μH)	220
	Stator Self-Inductance (μH)	20
	Permeant Magnetic Flux Linkage (Wb)	0.03
	Winding Shorted Path Resistance (mΩ)	1.3
	Shorted Turn Ratio (%)	0 to 1
Inverter	DC Bus Voltage (V)	48
	Switching Frequency (kHz)	2
Controller Setting	Control Sampling Frequency (kHz)	20
	Controller Outer-loop Proportional Gain	60
	Controller Outer-loop Integral Gain	600
	Controller Inner-loop I_q Proportional Gain	0.1
	Controller Inner-loop I_q Integral Gain	10
	Controller Inner-loop I_d Proportional Gain	0.1
	Controller Inner-loop I_d Integral Gain	10

Figure 5.11 showcases the SPMSM model is controlled by a realistic inverter gate signal under zero-fault condition. Its simulation results are presented in Figure (5.12) through (5.14), demonstrate the model's behavior as the shorted turn ratio is progressively adjusted from a healthy SPMSM condition (0%) to 5% and 15%, while the shorted path resistance is maintained at same value across all scenarios. Notably, 15% shorted turn ratios represent a very large inter-turn fault.

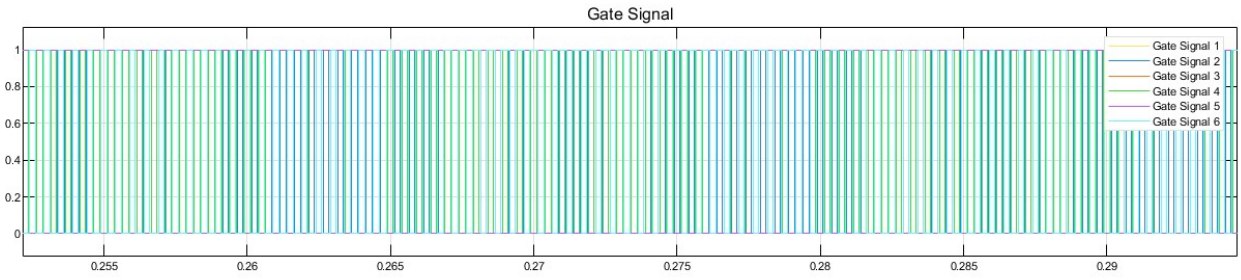

Figure 5.11 Model SVPWM controlled inverter gate signal

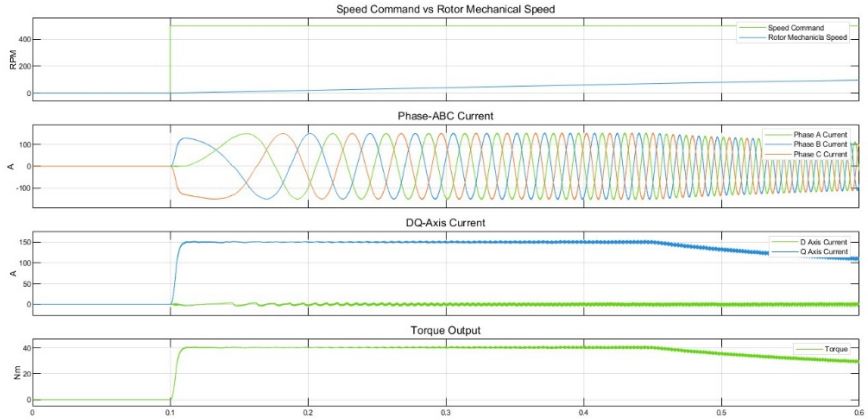

(a)

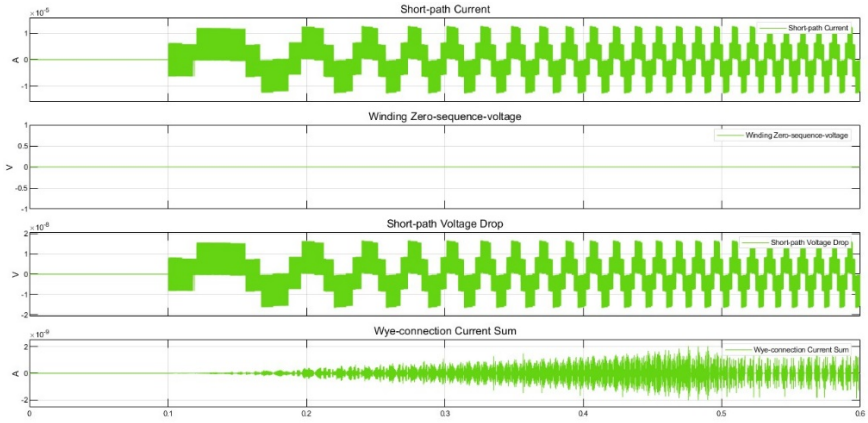

(b)

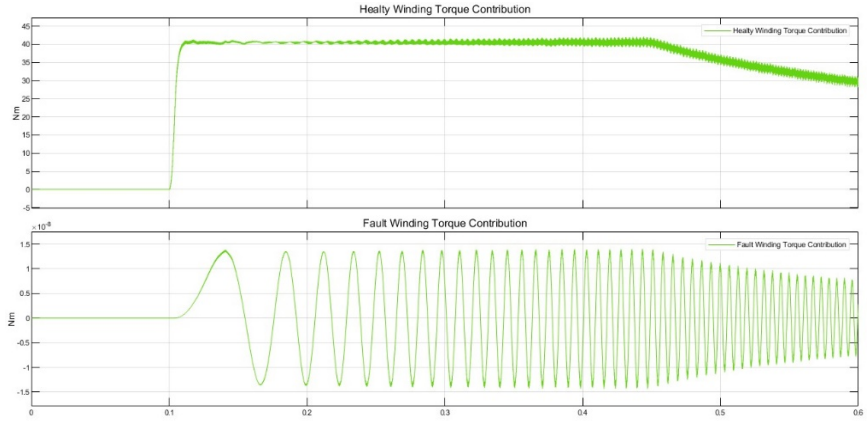

(c)

Figure 5.12 Result of the proposed simulation model at healthy condition.

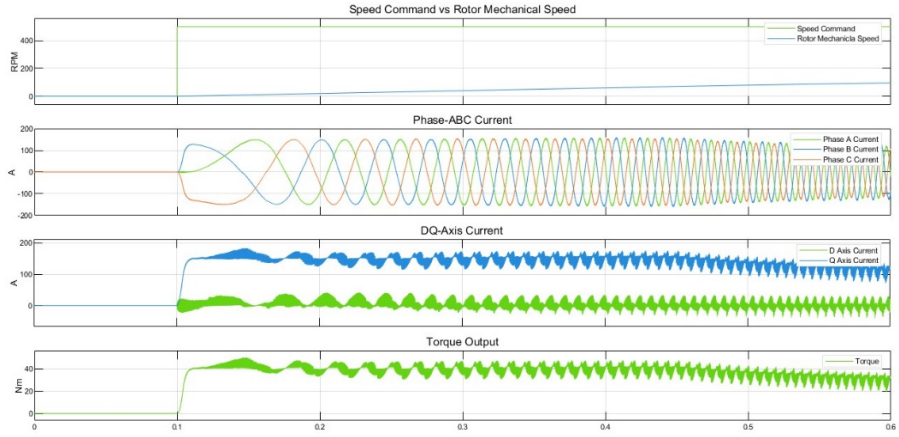

(a)

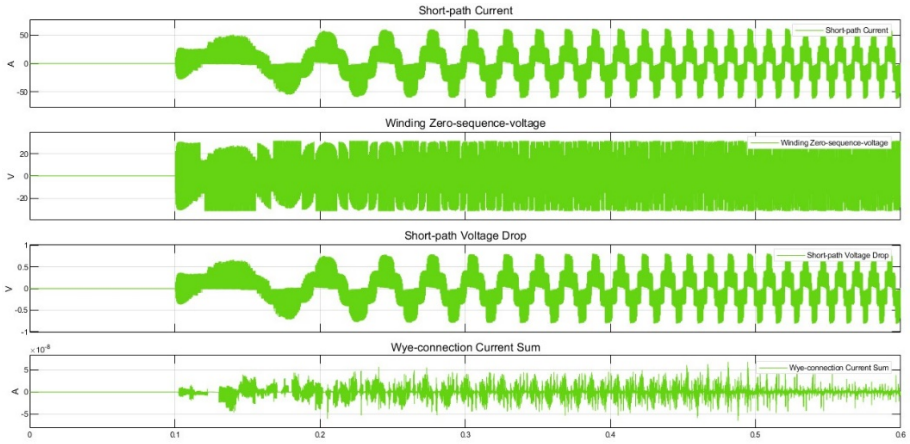

(b)

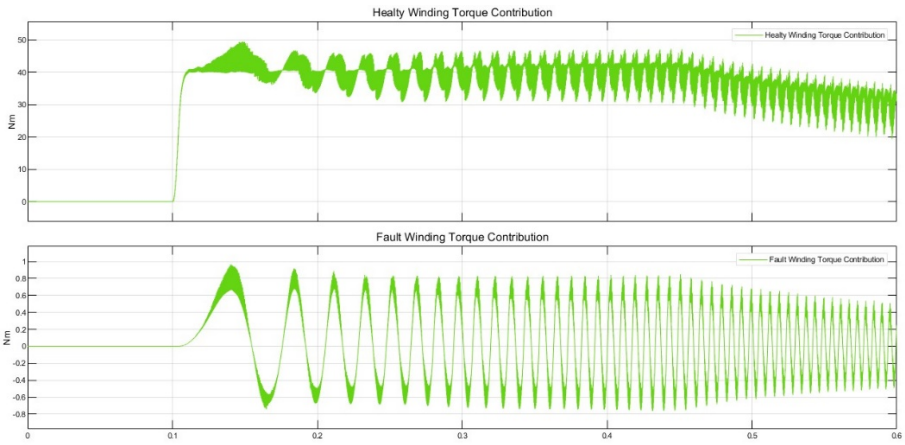

(c)

Figure 5.13 Result of the proposed simulation model at 5% condition.

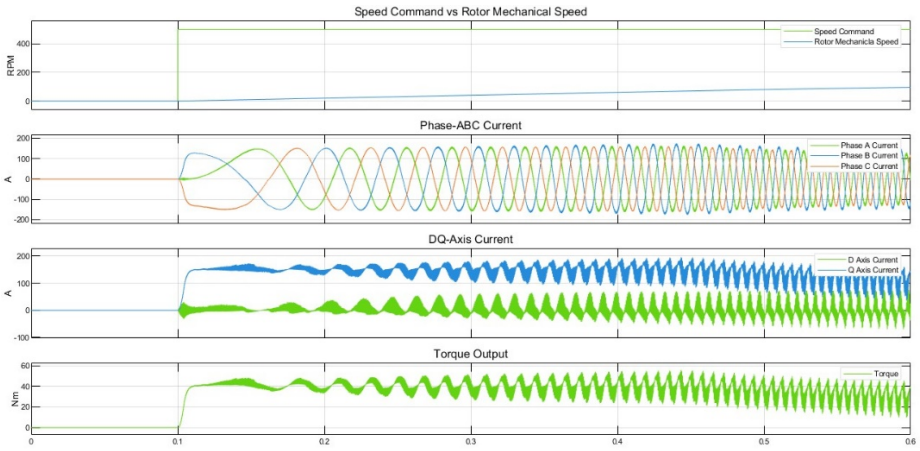

(a)

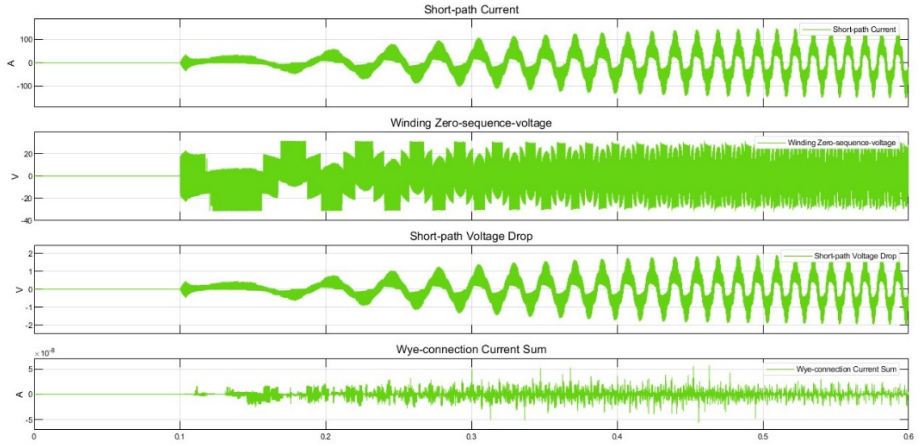

(b)

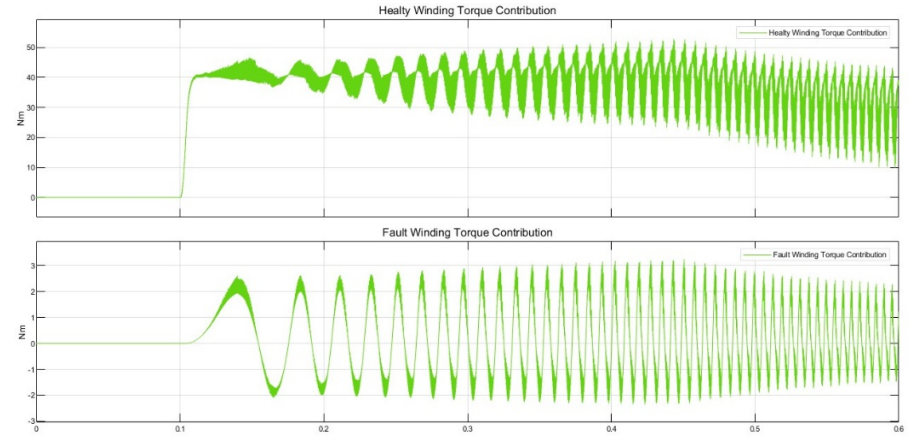

(c)

Figure 5.14 Result of the proposed simulation model at 15% condition.

From Figure 5.12, 5.13, 5.14 (a), it can be observed that as the rotor speed climbs towards its commanded value, the frequency of the three-phase current increases, maintaining a perfectly balanced state for the healthy SPMSM. The amplitude of the three-phase current remains constant while the speed is below the flux-weakening speed threshold. Once the speed surpasses this threshold, the amplitude of the three-phase current begins to decrease, concurrently with its torque output, and correspondingly, the *q*-axis current, as detailed in Chapter 5.2. For controlling the SPMSM, the q-axis current is typically maintained at zero, as further elaborated in pervious Chapter 5.2.1.

From Figure 5.12 (b), it can be observed that the zero-sequence voltage is precisely maintained at zero, as expected for a perfectly balanced machine. The minor variations in the Wye-connection current sum, which are at a negligibly low value, are attributable to numerical artifacts stemming from the Simulink step size, solver residue and numerical floating-point Errors.

As the shorted turn ratio increases from 0% to 5% and then to 15%, it is distinctly observable that the zero-sequence voltage exhibits significantly larger variations in amplitude. This directly indicates a more pronounced neutral point potential drift within the wye-connected machine windings, a consequence of the machine's inherent winding imbalance due to the fault. This escalating zero-sequence voltage variation serves as a critical hard fault indicator, as previously detailed in Chapter 3.2. Concurrently, another introduced fault indicator manifests as an increase in higher-order harmonics injected into the q-axis current as the shorted turn ratio rises. In a healthy (zero fault) state, the q-axis current is nearly a DC value. This transition to significant harmonic content with increasing fault severity is illustrated in Figures Figure 5.12 (b), Figure 5.13 (b), and Figure 5.14 (b).

Lastly, Figure 5.12 (c), Figure 5.13 (c), and Figure 5.14 (c) also suggest that an increased ripple presence in the q-axis current directly correlates with a larger torque ripple in the SPMSM. The total torque can be decomposed into two distinct contributions: the healthy winding torque and the fault winding torque. For the healthy winding torque contribution, its calculation remains consistent with that of a healthy SPMSM, as outlined in previously stated Equation (4.46), (4.47). In this component, the torque ripple primarily originates from the q-axis current ripple. On top of this, additional torque ripple is introduced from the fault winding torque contribution, the calculation of which is presented in Equation (4.57).

Chapter 6
Machine Learning Model Training

When the proposed simulation model is employed for machine learning (ML) model training in inter-turn fault detection, a significant advantage arises from its ability to consistently integrate controller action within the simulated environment. Unlike approaches that might attempt to abstract or isolate the controller, this methodology ensures that the controller's dynamic response is inherently included in each simulation iteration used for data generation. By running the model extensively (hundreds or thousands of times) for ML model training, the consistent influence of the controller on fault indicators is maintained. This consistency allows the machine learning algorithm to discern and capture the distinct patterns and subtle signatures introduced by inter-turn short faults, even amidst the controller's ongoing operation. Consequently, this approach facilitates the development of a highly accurate inter-turn short fault detection model capable of operating effectively in real-world closed-loop systems.

The SPMSM Simscape component, in conjunction with its Simulink controller setup developed in this research, was utilized in another independent research conducted by Akhila Chitturi. This particular research focused on training an ML model specifically to detect inter-turn short faults. While currently an unpublished work, this paper is referenced and summarized within this chapter to further demonstrate the substantial potential of the proposed simulation method in the context of training robust ML fault detection models.

6.1 Comparative Evaluation of CNN, Random Forest, and XGBoost for PMSM Fault Diagnosis Using Idc and Multi-Current Signals. [45]

This paper evaluates machine learning models for fault diagnosis in Permanent Magnet Synchronous Motors (PMSMs) using current signals from a Simulink-based simulation model. The dataset includes measurements of six electrical currents (i_{dc}, i_b, i_c, i_d, i_q, and I_{dc}) collected

over a consistent time interval, with varying fault turn ratios, winding resistance, and self-inductance. The study focuses on three classification models: Convolutional Neural Network (CNN), Random Forest (RF), and XGBoost. These models were trained and tested using two input configurations: (1) only the I_{dc} signal, and (2) all six currents.

A fixed time interval of 0.4 to 0.5 seconds was chosen for signal comparison consistency, as it contained the most prominent and stable fault characteristics. Fault severity was controlled by adjusting the fault turn ratio, while electrical variations were incorporated through changes in winding resistance and self-inductance. The dataset was constructed from 100 unique simulations, each representing a distinct combination of fault and electrical parameters. Fault turn ratios were varied across four levels: 0.0 (healthy), 0.1 (light), 0.2 (medium), and 0.3 (heavy). Winding resistance and self-inductance values were also adjusted to capture a wide spectrum of motor behavior.

In experiments using only the Idc signal without resampling, both convolutional networks showed a modest accuracy of 45%. In contrast, the Random Forest achieved 85% accuracy, and XGBoost reached 90%, indicating that hand-crafted statistics captured most of the Idc's discriminative content. When a fixed input length was imposed, the shallow CNN's accuracy improved significantly, rising to 72% at 1000 samples and peaking at 75% at 1200 samples. However, increasing samples to 1500 degraded performance to 60%. The deeper CNN did not match the shallow one, plateauing at 65% for 1000- and 1200-sample inputs and slipping to 55% at 1500 samples.

When the full set of phases and *dq* currents was introduced, CNN-2 reached 75% accuracy, while CNN-3 remained at 65%. The Random Forest model's accuracy increased to 95%, and XGBoost settled at 90%. Resampling multi-current traces to 1000 or 1200 samples did not improve

CNN performance, with CNN-2 at 75% and CNN-3 at 70%. The hybrid network generally failed to improve performance.

For binary fault classification, the models were trained and validated on data corresponding to two selected fault levels. Combinations involving smaller fault-turn ratios were flawlessly identified by all strong models. The combination (0.1, 0.2) remained challenging but acceptable, with CNN-2 achieving 90% accuracy on both single-current and multi-current versions, while Random Forest lagged slightly behind at 80%. The subtlest combination (0.2, 0.3) was the primary source of error, with the shallow CNN reaching only 60% accuracy, XGBoost edging up to 70% with Idc alone, and Random Forest reaching 70% only when all currents were provided.

As attached in Figure 6.1 showing comparison between single current and multiple current trained results, the paper concludes that resampling I_{dc} to 1200 points and training a two-convolution-block CNN yielded the most balanced outcome among deep models, providing a three-quarter classification rate without feature engineering. For maximum accuracy across all current channels, Random Forest was the algorithm of choice at 95%, with XGBoost close behind. The deeper CNN offered no advantage and often suppressed informative peaks. Therefore, XGBoost is recommended for I_{dc}-only deployments where statistical heterogeneity needs to be captured from a single channel, and Random Forest for multi-channel diagnostics that prioritize accuracy and interpretability. A lightweight, two-convolution-block CNN remains attractive when real-time, on-board execution and minimal feature engineering are priorities.

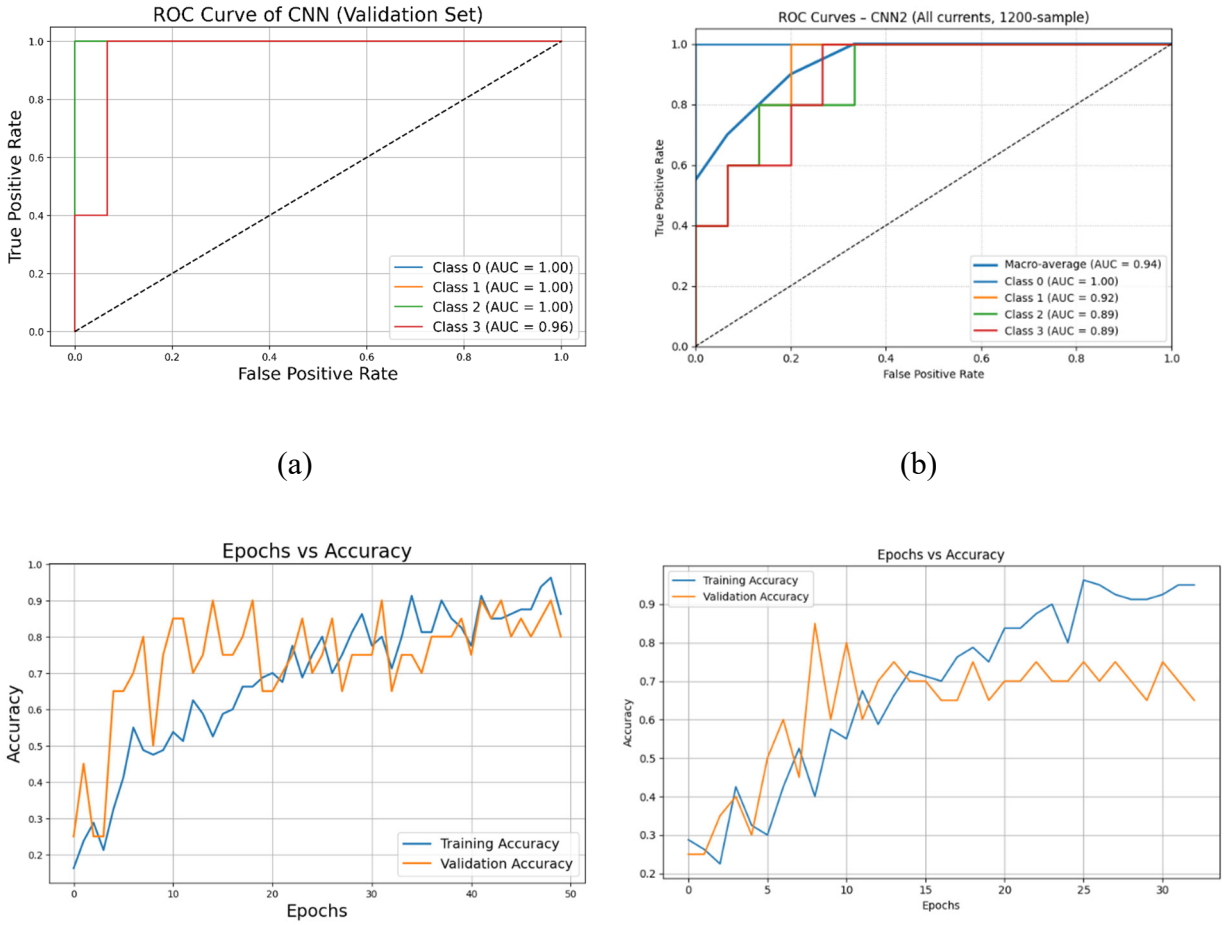

Figure 6.1 Receiver Operating Characteristic curve for CNN2 trained on (a) Idc only data (b) all currents data resampled to 1200 samples. Training and validation accuracy curves for CNN2 trained on (c) Idc only data (d) all currents data resampled to 1200 samples.

Chapter 7

Conclusion and Recommended Future Work

6.1 Conclusions

The scope of this work was to develop robust numerical efficient simulation model for PMSMs under inter-turn short fault condition, specifically tailored for machine learning-based fault detection in traction drive applications. leveraging Simscape's acausal syntax and implicit DAE solver, a novel modeling framework was developed. This approach effectively resolved the complexities associated with expanding the machine's governing equations to incorporate fault dynamics, avoiding numerical instability and algebraic loops commonly encountered in traditional simulation environments.

The proposed SPMSM model, integrated within a FOC control with SVPWM, demonstrated high fidelity and computational efficiency. Simulation results validated its ability to accurately capture the characteristic fault indicators, such as the increasing amplitude of zero-sequence voltage and the emergence of higher-order harmonics in dq-axis currents, as the inter-turn fault severity increased. The model's ability to consistently integrate controller actions within the simulated environment is a significant advantage, ensuring that generated data realistically reflects real-world operating conditions.

As demonstrated by the referenced independent research utilizing this simulation model, the framework proved highly effective for training various machine learning algorithms. The comparative evaluation highlighted the strengths of Random Forest and XGBoost for multi-channel and single-channel fault diagnosis, respectively, achieving high classification accuracies (up to 95%). A lightweight Convolutional Neural Network also showed promising results for scenarios prioritizing real-time, on-board execution with minimal feature engineering. This validates the core hypothesis that a high-speed, accurate, and scalable simulation model is crucial for developing reliable machine learning-driven fault detection systems.

6.2 Contributions

This research focused on developing a robust model for stator winding inter-turn faults. A key contribution of this work is the formulation of a comprehensive and accurate model capable of simulating the complex behavior of such faults. The proposed model serves as a vital tool for analyzing fault phenomena in permanent magnet synchronous machines PMSMs and for training machine learning algorithms aimed at fault detection. The main contributions are summarized below:

- Establishment of theoretical foundation for both SPMSM and IPMSM:

  Based on principles from several published studies, a detailed dq-axis voltage governing equation for stator windings with inter-turn short faults was developed for both SPMSMs and IPMSMs. Several errors were identified in reviewed references, including an incorrectly defined Park transformation and improper handling of zero-sequence voltage in practical simulations, which rendered the original model non-functional. These issues were corrected, and the accurate voltage and torque equations, including fault-induced effects, were correctly derived and verified.

- Development of a Novel SPMSM Fault Model:

  This work presents a robust and numerically efficient inter-turn fault model for SPMSMs, developed in the Simulink–Simscape environment. By utilizing Simscape's implicit DAE solver, the model accurately captures fault-loop dynamics without requiring artificial delays or manual equation reformulation. It integrates seamlessly with closed-loop control systems, enabling stable, high-fidelity simulation under dynamic conditions. Compared to traditional models, it offers improved scalability and simulation speed,

making it well-suited for generating large datasets for machine learning-based fault detection using standard traction inverter signals. The model itself exhibits a high degree of flexibility, allowing for the integration of future machine-specific details. For instance, higher-order flux linkage harmonics can be incorporated using a lookup table (LUT), which facilitates the model's expansion for more detailed studies.

- Integrated Closed-Loop Simulation

  A comprehensive closed-loop simulation framework was developed to accurately represent the behavior of SPMSMs under inter-turn fault conditions. This framework integrates speed-controlled FOC and SVPWM to generate inverter gate signals from an inverter model, replicate realistic drive system operation, including dynamic responses to torque commands and control feedback interactions. By simulating the full control loop, the model captures the subtle effects of fault-induced asymmetries on both electrical and mechanical performance. This realistic simulation environment is essential for validating fault detection algorithms and ensures that model outputs closely reflect real-world operating conditions in traction applications.

- Enabling Machine Learning Training:

  The developed simulation platform offers both high computational speed and modeling accuracy, making it exceptionally well-suited for machine learning applications. It enables the efficient generation of large-scale, diverse datasets that reflect a wide range of operating conditions and fault scenarios. These datasets are critical for training advanced machine learning models aimed at inter-turn fault detection, especially when relying solely

on standard traction inverter signals such as phase currents. This approach supports the development of accurate, real-time, and hardware-compatible diagnostic systems.

6.3 Recommended Future Work

Building upon the foundations laid in this dissertation, several avenues for future research are recommended:

- IPMSM Model with Control:

  The developed modeling framework can be extended to fully incorporate the dynamic behavior of IPMSMs, based on the established theoretical foundation. The IPMSM model supports further enhancement by integrating advanced features, such as higher-order harmonics in the flux linkage by LUT. Building on this model, advanced control strategies can be implemented, including MTPA and flux weakening control, enabling accurate analysis and performance optimization across a wide speed range.

- Experimental Validation:

  Conduct experimental validation using a physical PMSM test bench to corroborate the simulation results and the performance of trained machine learning models in a real-world setting.

  To verify the accuracy and practical applicability of the proposed simulation framework, experimental validation using a physical PMSM test bench is recommended. This setup replicates real-world operating conditions, enabling direct comparison between simulated and measured responses under both healthy and faulted scenarios. Key performance indicators, such as current waveforms, torque response, and fault signatures,

can be evaluated to assess the model's fidelity. In addition, the trained machine learning models were deployed and tested using real-time sensor data from the bench, allowing for a thorough assessment of their fault detection capabilities and generalization performance in a realistic operating environment.

- Advanced Machine Learning Training:

  Explore and implement more advanced machine learning and deep learning architectures, such as Recurrent Neural Networks (RNNs) or Transformers, for time-series analysis of fault signatures, potentially leading to earlier and more accurate fault detection.

- Multi-Fault Scenarios:

  Investigate the modeling and detection of multiple simultaneous fault types (e.g., inter-turn fault combined with bearing fault) to enhance the diagnostic capabilities of the system.

- Hardware-in-the-Loop (HIL) Testing:

  Integrate the developed simulation model with real-time hardware-in-the-loop systems to test controller performance and fault detection algorithms under realistic operating conditions before full deployment.

REFERENCES

[1] X. Liu, W. Miao, Q. Xu, L. Cao, P. W. T. Pong, and C. Liu, "Inter-Turn Short-Circuit Fault Detection Approach for Permanent Magnet Synchronous Machines Through Stray Magnetic Field Sensing," IEEE Sensors Journal, vol. 19, no. 18, pp. 7844-7895, Sept. 2019.

[2] The Motor Reliability Working Group, P. F. Albrecht (Chairman), J. C. Das, D. W. Jackson, G. W. Buckley, and R. L. Doughty, "Report of Large Motor Reliability Survey of Industrial and Commercial Installations, Part I," *IEEE Transactions on Industry Applications*, vol. IA-21, no. 4, pp. 853-864, July 1985.

[3] Duke Electric, "3-phase winding failure examples," *Duke Electric Blog*. [Online]. Available: https://www.dukeelectric.com/blog/3-phase-winding-failure-examples/. [Accessed: Jun. 17, 2025].

[4] J. S. Sottile and J. L. Kohler, "An on-line method to detect incipient failure of turn insulation in random-wound motors," *IEEE Transactions on Energy Conversion*, vol. 8, no. 4, pp. 762-768, Dec. 1993.

[5] S. K. Sul, *Control of Electric Machine Drive Systems*. Hoboken, NJ, USA: Wiley-IEEE Press, 2011.

[6] R. M. Tallam, T. G. Habetler, and R. G. Harley, "Transient model for the detection of stator winding inter-turn faults in induction machines," in *Conference Record of the 2002 IEEE Industry Applications Conference. 37th IAS Annual Meeting*, Pittsburgh, PA, USA, 2002, vol. 1, pp. 369-374.

[7] B. A. Welchko, M. B. de Rossiter Correa, and T. A. Lipo, "Modeling of surface-mounted permanent magnet synchronous motors with stator winding interturn faults," *IEEE Transactions on Industry Applications*, vol. 40, no. 3, pp. 832-840, May-June 2004.

[8] B. A. Welchko, M. B. de Rossiter Correa, and T. A. Lipo, "Modeling of surface-mounted permanent magnet synchronous motors with stator winding interturn faults," *IEEE Transactions on Industry Applications*, vol. 40, no. 3, pp. 832-840, May-June 2004

[9] MathWorks, "Permanent Magnet Synchronous Motor with Interturn Fault," *MathWorks Help Center*. [Online]. Available: https://www.mathworks.com/help/sps/ug/motor-pmsm-faulted.html. [Accessed: Jun. 18, 2025].

[10] J. Rosero, A. G. Espinosa, J. Cusido, J. A. Ortega, and L. Romeral, "Simulation and fault detection of short circuit winding in a permanent magnet synchronous Machine (PMSM) by means of Fourier and wavelet transform," in *2008 IEEE Instrumentation and Measurement Technology Conference*, Victoria, BC, Canada, 2008, pp. 1319-1324.

[11] J. S. Sottile and J. L. Kohler, "An on-line method to detect incipient failure of turn insulation in random-wound motors," *IEEE Transactions on Energy Conversion*, vol. 8, no. 4, pp. 762-768, Dec. 1993.

[12] R. M. Tallam, T. G. Habetler, and R. G. Harley, "Transient model for the detection of stator winding inter-turn faults in induction machines," in *Conference Record of the 2002 IEEE Industry Applications Conference. 37th IAS Annual Meeting*, Pittsburgh, PA, USA, 2002, vol. 1, pp. 369-374.

[13] A. M. da Silva, R. J. Povinelli, and N. A. O. Demerdash, "Induction machine broken bar and stator short-circuit fault diagnostics based on three-phase stator current," in *2008 IEEE Power and Energy Society General Meeting - Conversion and Delivery of Electrical Energy in the 21st Century*, Pittsburgh, PA, USA, 2008, pp. 1-8

[14] W. T. Thomson and M. Fenger, "Current signature analysis to detect induction motor faults," *IEEE Industry Applications Magazine*, vol. 7, no. 4, pp. 26-34, Jul./Aug. 2001.

[15] M. Riera-Guasp, J. A. Antonino-Daviu, M. Pineda-Sanchez, R. Puche-Panadero, and J. Perez-Cruz, "A general approach for the transient detection of slip-dependent fault components in induction machines," *IEEE Transactions on Industrial Electronics*, vol. 55, no. 12, pp. 4167-4180, Dec. 2008.

[16] J. S. Sottile and J. L. Kohler, "An on-line method to detect incipient failure of turn insulation in random-wound motors," *IEEE Transactions on Energy Conversion*, vol. 8, no. 4, pp. 762-768, Dec. 1993.

[17] J. S. Sottile and J. L. Kohler, "An on-line method to detect incipient failure of turn insulation in random-wound motors," *IEEE Transactions on Energy Conversion*, vol. 8, no. 4, pp. 762-768, Dec. 1993.

[18] M. A. Awadallah and M. M. Morcos, "Application of symmetrical components and wavelet transforms for fault diagnosis in a permanent magnet synchronous motor," *IEEE Transactions on Energy Conversion*, vol. 19, no. 4, pp. 696-703, Dec. 2004.

[19] J.-H. Im, J.-H. Kim, J.-M. Kim, S.-W. Kim and J.-R. Jung, "Diagnosis of inter-turn short circuit in windings of permanent magnet synchronous motor," in *2007 International Conference on Electrical Machines and Systems (ICEMS)*, Seoul, Korea (South), 2007, pp. 782-786.

[20] D. G. Dorrell, N. T. D. Hieu and M. A. El-Refaie, "Diagnosis of stator winding inter-turn short-circuit faults in permanent-magnet synchronous machines: The impact of inherent machine asymmetries," *IEEE Transactions on Magnetics*, vol. 49, no. 7, pp. 3479-3482, July 2013.

[21] A. M. E. A. El-Maleh, "A study of the effects of turn-to-turn short-circuit fault on the performance of permanent magnet synchronous motor," in *2015 IEEE International Conference on Industrial Technology (ICIT)*, Seville, Spain, 2015, pp. 1913-1918.

[22] G. K. Singh and A. S. Al-kazzaz, "Induction machine drive condition monitoring and diagnostic techniques—a review," *Electric Power Systems Research*, vol. 64, no. 2, pp. 145-158, Feb. 2003.

[23] D. Lee, J. K. Park, and J. M. Kim, "Stator winding fault diagnosis of a permanent magnet synchronous motor by using a line-neutral voltage," in *2010 IEEE International Symposium on Industrial Electronics*, Bari, Italy, 2010, pp. 2975-2980.

[24] H. A. Toliyat and T. A. Lipo, "Transient analysis of cage induction machines under stator, rotor, and eccentric faults," *IEEE Transactions on Energy Conversion*, vol. 10, no. 2, pp. 241-247, June 1995.

[25] D. E. Schump, “Predict motor failure with insulation testing,” in *Pulp and Paper Industry Technical Conference, 1997*, Cincinnati, OH, USA, 1997, pp. 48-50.

[26] D. E. Schump, “Reliability testing of electric motors,” *IEEE Transactions on Industry Applications*, vol. 25, no. 3, pp. 386-390, May/June 1989.

[27] R. Maier, “Protection of squirrel-cage induction motor utilizing instantaneous power and phase information,” *IEEE Transactions on Industry Applications*, vol. 28, no. 2, pp. 376-380, Mar./Apr. 1992.

[28] J. S. Hsu, “Monitoring of defects in induction motors through air-gap torque observation,” *IEEE Transactions on Industry Applications*, vol. 31, no. 5, pp. 1016-1021, Sept./Oct. 1995.Sept./Oct., 1995.

[29] L. Stankovic, S. Stankovic, and I. Djurovic, "On Some Spectrum Estimation Methods for Analysis of Non-stationary Signals in Power Systems Part I: Theoretical Aspects," *European Transactions on Electrical Power*, vol. 9, no. 1, pp. 45-52, Jan./Feb. 1999.

[30] L. Stankovic, I. Djurovic, and S. Stankovic, "Advanced Signal Processing Methods for Analysis of Non-stationary Signals in Power Systems," in *Power Quality: Mitigation Technologies in a Distributed Environment*, A. Moreno-Munoz, Ed. London: Springer, 2007, pp. 233-274.

[31] G. Rouleau, "Why You Should Never Break an Algebraic Loop with a Memory Block," *The Simulink Blog*, Jul. 18, 2015. [Online]. Available: https://blogs.mathworks.com/simulink/2015/07/18/why-you-should-never-break-an-algebraic-loop-with-with-a-memory-block/. [Accessed: Jun. 18, 2025].

[32] Y. Lee and T. G. Habetler, "A phase variable simulation model for interior PM synchronous motor drives with stator turn faults," in *2005 IEEE International Symposium on Industrial Electronics*, Dubrovnik, Croatia, 2005, pp. 1017-1022.

[33] MathWorks, "Choose an ODE Solver," *MathWorks Help Center*. [Online]. Available: https://www.mathworks.com/help/matlab/math/choose-an-ode-solver.html. [Accessed: Jun. 18, 2025].

[34] MathWorks, "Choose an ODE Solver," *MathWorks Help Center*. [Online]. Available: https://www.mathworks.com/help/matlab/math/choose-an-ode-solver.html. [Accessed: Jun. 18, 2025].

[35] MathWorks, "About Simscape Files," *MathWorks Help Center*. [Online]. Available: https://www.mathworks.com/help/simscape/lang/about-simscape-files.html. [Accessed: Jun. 18, 2025].

[36] MathWorks, "acuasal modelling," *MATLAB Central Answers*. [Online]. Available: https://www.mathworks.com/matlabcentral/answers/17242-acuasal-modelling. [Accessed: Jun. 18, 2025].

[37] Roboteq, "Field Oriented Control (FOC) Made Ultra Simple," *Roboteq*. [Online]. Available: https://www.roboteq.com/applications/all-blogs/13-field-oriented-control-foc-made-ultra-simple. [Accessed: Jun. 18, 2025].

[38] J. Song, "Flux weakening control of surface mounted permanent magnet synchronous motor," Ph.D. dissertation, Seoul National University, Seoul, Korea, 1996 (in Korean).

[39] S. K. Sul, *Control of Electric Machine Drive Systems*. Hoboken, NJ, USA: Wiley-IEEE Press, 2011.

[40] A. Aktaş and Y. Kirçiçek, *Solar Hybrid Systems*. 2021.

[41] A. Schönung and H. Stemmler, "Static frequency changers with subharmonic control in conjunction with reversible variable-speed A.C. drives," *Brown Boveri Review*, vol. 51, pp. 555-577, 1964.

[42] H. W. van der Broeck, H. C. Skudelny, and G. V. Stanke, "Analysis and realization of a pulsewidth modulator based on voltage space vectors," in *Conference Record of the 1986 IEEE Industry Applications Society Annual Meeting*, 1986, pp. 244-251.

[43] J. W. Kolar, H. Ertl, and F. C. Zach, "Influence of the modulation method on the conduction and switching losses of a PWM inverter system," *IEEE Transactions on Industry Applications*, vol. 27, no. 6, pp. 1063-1075, Nov./Dec. 1991.

[44] A. M. Hava, R. J. Kerkman, and T. A. Lipo, "A high-performance generalized discontinuous PWM algorithm," *IEEE Transactions on Industry Applications*, vol. 34, no. 5, pp. 1059-1071, Sept./Oct. 1998.

[45] A. Chitturi and T. Kim, "Comparative Evaluation of CNN, Random Forest, and XGBoost for PMSM Fault Diagnosis Using Idc and Multi-Current Signals," Dept. of Electrical and Computer Engineering, University of Michigan - Dearborn, Dearborn, USA, unpublished.

Appendices

```
component AdjustableTurnFaultSMPMSM
    % SMPMSM Model with Interturn Fault V2.3
    %
    %
    % Rev2.3 Fixed u=0 issue, V0 cannot be directly calculated from the simscape model since any .der term will be considered constraining equation
    % Line 113 V_0 is not valid becase it is directlly park transfered from Vabc.
    % Vabc is perfectly balance even there is internal fault in motor. because it comes from inverter voltage source
    % Therefor V_0 cannot represent ZSV, equation [(-1/3)*u*Rs*i_f - (1/3)*u*(L+2*M)*(i_f.der);] need to be used to calculate winding voltage drop

    parameters
        % nPolePairs =  {6, '1'};             % Number of pole pairs
        % pm_flux_linkage = {0.03, 'Wb'};    % Permanent magnet flux linkage
        % L = {0.00022, 'H'};                % Self inductance, L
        % M = {0.00002, 'H'};                % Mutual inductance, M
        % Rs = {0.013, 'Ohm'};                % Stator resistance per phase, Rs
        % Rf = {0.013, 'Ohm'};                % Fault turn resistance, Rf
        % f_ratio = {0.1, '1'}                      % Fault turn ratio
    end

    parameters (Access=protected)
        shift_3ph = { [0,-2*pi/3,2*pi/3], 'rad' };
    end

    nodes
        N = foundation.electrical.three_phase;           % ~:left
        R = foundation.mechanical.rotational.rotational; % R:right
        C = foundation.mechanical.rotational.rotational; % C:right
    end

    inputs
        nPolePairs =  {0, '1'};             % Number of pole pairs
        pm_flux_linkage = {0.0, 'Wb'};    % Permanent magnet flux linkage
        L = {0.0, 'H'};                % Self inductance, L
        M = {0.0, 'H'};                % Mutual inductance, M
        Rs = {0.0, 'Ohm'};                % Stator resistance per phase, Rs
        Rf = {0.0, 'Ohm'};                % Fault turn resistance, Rf
        f_ratio = {0.0, '1'}                      % Fault turn ratio
    end

    variables (Access = protected)
        % Mechanical
        angular_position_diff = {0, 'rad'}; % Rotor angle wrt synchronous reference frame

        f_i_d = {0, 'A'}; % fault d-axis current
        f_i_q = {0, 'A'}; % fault q-axis current
        i_f = {0, 'A'}; % fault current


        %Protected variable
        % Mechanical
        f_torque = {0, 'N*m' }; % Mechanical torque
        f_torque_h = {0, 'N*m' }; % Healthy part torque contribution
        f_torque_f = {0, 'N*m' }; % Fault part torque contribution

        % Stator currents
        I = {[0 0 0], 'A' }; % Phase currents [Ia Ib Ic]
        I_fault = {[0 0 0 0], 'A' }; % Phase currents including If [Ia Ib Ic If]

    end
```

```
outputs

    f_i_a_out = {0, 'A'}; % fault a current
    f_i_b_out = {0, 'A'}; % fault b current
    f_i_c_out = {0, 'A'}; % fault c current

    f_i_d_out = {0, 'A'}; % fault d current
    f_i_q_out = {0, 'A'}; % fault q current

    Iabc_out = {0, 'A'}; % abc phase current sum

    i_f_out = {0, 'A'}; % fault path current
    vf_out = {0, 'V'}; % fault path voltage drop

    f_torque_out = {0, 'N*m'}; % Fault torque output
    f_torque_h_out = {0, 'N*m'}; % Healthy part torque contribution output
    f_torque_f_out = {0, 'N*m'}; % Fault part torque contribution outpu

end

branches
    I      : N.I    -> *;
    f_torque : R.t -> C.t;
end

equations
    let

        angular_velocity = R.w - C.w;
        electrical_angle = nPolePairs*angular_position_diff;
        electrical_angle_vec = electrical_angle+shift_3ph;

        abc2dq = 2/3*[...
                cos( electrical_angle_vec );...
                -sin( electrical_angle_vec )];

        dq2abc = [...
                cos(electrical_angle_vec(1)) -sin(electrical_angle_vec(1));...
                cos(electrical_angle_vec(2)) -sin(electrical_angle_vec(2));...
                cos(electrical_angle_vec(3)) -sin(electrical_angle_vec(3))];

        abcf2dq0f = 2/3*[cos( electrical_angle_vec(1) ) cos( electrical_angle_vec(2) ) cos( electrical_angle_vec(3) ) cos( electrical_angle_vec(1) );...
                -sin( electrical_angle_vec(1) ) -sin( electrical_angle_vec(2) ) -sin( electrical_angle_vec(3) ) -sin( electrical_angle_vec(1) );...
                1/2 1/2 1/2 0;...
                0 0 0 3/2];

        dq0f2abcf = [cos( electrical_angle_vec(1) ) -sin( electrical_angle_vec(1) ) 1 -2/3;...
                cos( electrical_angle_vec(2) ) -sin( electrical_angle_vec(2) ) 1 1/3;...
                cos( electrical_angle_vec(3) ) -sin( electrical_angle_vec(3) ) 1 1/3;...
                0 0 0 1];

        vdq0f = abcf2dq0f*[N.V 0]';
        f_vd = vdq0f(1);
        f_vq = vdq0f(2);
        % =============
        % f_v0 = vdq0f(3);
        % This is not valid representation
        % =============
        % vf = vdq0f(4);

        u = max(f_ratio, 1e-9); % Add ratio lower limit to prevent zero dividing issue

        f_vdh = (3+u+u*cos(2*electrical_angle))*(1/3)*Rs*f_i_d...
                -(3+u+u*cos(2*electrical_angle))*(1/3)*(L-M)*(nPolePairs*angular_velocity)*f_i_q...
                +(3+u+u*cos(2*electrical_angle))*(1/3)*(L-M)*(f_i_d.der);

        f_vqh = pm_flux_linkage*nPolePairs*angular_velocity...
                +(3+u-u*cos(2*electrical_angle))*(1/3)*Rs*f_i_q...
                +(3+u-u*cos(2*electrical_angle))*(1/3)*(L-M)*(nPolePairs*angular_velocity)*f_i_d...
                +(3+u-u*cos(2*electrical_angle))*(1/3)*(L-M)*(f_i_q.der);
```

```
        f_vdf = -(2/9)*cos(electrical_angle)*(3*Rf+Rs*(3+8*u))*i_f...
                -(2/3)*cos(electrical_angle)*sin(electrical_angle)*Rs*u*f_i_q...
                -(1/3)*(L-M)*(nPolePairs*angular_velocity)*u*sin(2*electrical_angle)*f_i_d...
                -(2/9)*cos(electrical_angle)*(-M*(3+5*u)+L*(3+5*u+3*(u^2)))*(i_f.der)...
                -(2/3)*cos(electrical_angle)*sin(electrical_angle)*(L-M)*u*(f_i_q.der);

        f_vqf = -(2/3)*cos(electrical_angle)*sin(electrical_angle)*Rs*u*f_i_d...
                +(2/9)*sin(electrical_angle)*(3*Rf+Rs*(3+8*u))*i_f...
                -(1/3)*(L-M)*(nPolePairs*angular_velocity)*u*sin(2*electrical_angle)*f_i_q...
                -(1/3)*(L-M)*u*sin(2*electrical_angle)*(f_i_d.der)...
                +(2/9)*sin(electrical_angle)*(-M*(3+5*u)+L*(3+5*u+3*(u^2)))*(i_f.der);


    in

        angular_velocity == angular_position_diff.der;

        f_vd == f_vdh + f_vdf;
        f_vq == f_vqh + f_vqf;

        Rf*i_f == (Rs*u*cos(electrical_angle)-(L-M)*u*nPolePairs*angular_velocity*sin(electrical_angle))*f_i_d...
                  -(Rs*u*sin(electrical_angle)+(L-M)*u*nPolePairs*angular_velocity*cos(electrical_angle))*f_i_q...
                  -(1/3)*(3*Rf+5*Rs*u)*i_f...
                  +(L-M)*u*cos(electrical_angle)*(f_i_d.der)...
                  -(1/3)*u*(-2*M+L*(2+3*u))*(i_f.der)...
                  -(L-M)*u*sin(electrical_angle)*(f_i_q.der)...
                  -u*pm_flux_linkage*nPolePairs*angular_velocity*sin(electrical_angle);


        I' == dq2abc*[f_i_d;f_i_q];

        I_fault' == dq0f2abcf * [f_i_d; f_i_q; 0; i_f];

        % Don't need current balancing queation I_fault(1)+I_fault(2)+I_fault(3) == 0, Idq = [Id Iq I0 If]: I0 = 0 in wye no homopolar current

        f_torque == f_torque_h + f_torque_f;
        f_torque_h == 3/2*nPolePairs*f_i_q*pm_flux_linkage;
        f_torque_f == (3/2)...
                    *(f_i_d*(-(1/3)*(L-M)*(nPolePairs)*u*sin(2*electrical_angle)*f_i_d)...
                    +f_i_q*(-(1/3)*(L-M)*(nPolePairs)*u*sin(2*electrical_angle)*f_i_q));



        f_i_a_out == I_fault(1);
        f_i_b_out == I_fault(2);
        f_i_c_out == I_fault(3);
        i_f_out == I_fault(4);
        f_i_d_out == f_i_d;
        f_i_q_out == f_i_q;
        vf_out == Rf*i_f;
        f_torque_out == f_torque;
        f_torque_h_out == f_torque_h;
        f_torque_f_out == f_torque_f;
        Iabc_out == I_fault(1) + I_fault(2) + I_fault(3);

    end
end

end
```